Theory of the nanoscale surface ripples produced by ion irradiation of a miscut (001) gallium arsenide surface

Tejas Sharath
Department of Physics, Colorado State University, Fort Collins, Colorado 80523, USA

R. Mark Bradley
Departments of Physics and Mathematics, Colorado State University, Fort Collins, Colorado 80523, USA

(Received 8 September 2021; revised 11 January 2022; accepted 6 February 2022; published 22 February 2022)

We develop a theory for the surface ripples produced by near-normal-incidence ion bombardment of a (001) GaAs surface with a small miscut along the [110] direction. We restrict our attention to the case in which the energy of the incident ions is below the sputter yield threshold and the sample temperature is just above the recrystallization temperature. Highly ordered, faceted ripples with their wave vector aligned with the [110] direction form when the ion beam is normally incident and there is no miscut. Two additional terms appear in the equation of motion when the beam is obliquely incident and/or there is a miscut: a linearly dispersive term and a nonlinearly dispersive term. The coefficients of these terms can become large as the threshold temperature for pattern formation is approached from above. In the absence of strong nonlinear dispersion, strong linear dispersion leads to ripples with a dramatically increased degree of order. These ripples are nearly sinusoidal even though they are on the surface of a single crystal. The exceptionally high degree of order is disrupted by nonlinear dispersion if the coefficient of that term is sufficiently large. However, by choosing the angle of ion incidence appropriately, the coefficient of the nonlinearly dispersive term can be made small. Ion bombardment will then produce highly ordered ripples. For a different range of parameter values, nucleation and growth of facets and spinodal decomposition can occur.

DOI: 10.1103/PhysRevE.105.024801

I. INTRODUCTION

Bombarding a solid surface with a broad ion beam can produce a variety of self-assembled nanoscale patterns, including surface ripples and hexagonal arrays of mounds [1–6]. The spontaneous formation of these patterns is not just fascinating in its own right: ion bombardment has the potential to become a cost-effective method to rapidly fabricate large-area nanostructures with features smaller than those that can be produced by conventional optical lithography. The patterns that form, however, are typically rife with defects, and this has been a longstanding issue in this field. This problem has been the primary obstacle that has prevented the widespread use of ion bombardment as a nanofabrication tool, and a great deal of work has been done with the goal of producing defect free patterns [7–21].

In 2015, Ou *et al.* reported a dramatic breakthrough in this quest: ripples with a remarkably high degree of order emerged when a GaAs (001) surface was bombarded with a normally-incident 1 keV argon ion beam and the sample was maintained at a temperature T above its recrystallization temperature T_R [14,22]. Ripples of this kind have subsequently been employed in a maskless, high-throughput method to fabricate multilayer blazed diffraction gratings with periods in the sub-50 nm range [23].

Ou *et al.* also introduced a phenomenological theory that is able to at least partially account for the pattern formation they observed [14]. In their theory, the role of the incident ions is simply to produce vacancies in the crystal surface. These vacancies diffuse on the crystal terraces until they attach to a step edge. Ou *et al.* assumed that the slope dependence of the sputter yield can be neglected [14]. They also assumed that the ratio of gallium atoms to arsenic atoms remains one-to-one even though one of the two atomic species would have been preferentially sputtered. These assumptions are unnecessary, however, if the energy of the incident ions is on the order of a few tens of electron volts since in this low-energy regime, sputtering is negligible. Experiments in this regime have already been carried out by Chowdhury and Ghose, who bombarded a GaAs (001) surface with a normally-incident 30 eV argon ion beam while the sample was held at a temperature $T > T_R$ [24]. The formation of well ordered ripples was observed, although the order was not as strong as in the higher energy experiments of Ou *et al.* [14]. Chowdhury and Ghose also found that ripples formed for temperatures T above a critical temperature $T_{c,0}$, whereas the surface remained flat for $T < T_{c,0}$ [24].

In this paper, a theory for the pattern formation that occurs when the surface of a GaAs single crystal is bombarded with a near-normally-incident, low-energy noble gas ion beam is developed. We consider both (001) surfaces and (001) surfaces with a small miscut along the [110] direction and focus on temperatures T close to the threshold temperature for pattern formation $T_{c,0}$.

The equation that is found to govern the surface dynamics of a (001) surface is identical to the one Ou *et al.* arrived at using phenomenological arguments. In this case, ion bombardment produces highly ordered, faceted ripples with their wave vector aligned with the [110] direction. These ripples are not perfectly ordered, however, since their wavelength can vary along the [110] direction.

Our motivation for studying the effect of a miscut is that there are *a priori* reasons to believe that ion bombardment of a miscut surface could produce an even higher degree of order than bombarding a surface without a miscut. Two additional terms appear in the equation of motion (EOM) when there is a miscut. One of these is a linearly dispersive term, and strong linear dispersion has been shown to engender a high degree of order in other contexts [18,20,25]. Consistent with this, we find that when the coefficient of this term (γ) is large, ripples develop with a higher degree of order than for $\gamma = 0$. Our simulations and analytical work establish that these ripples are not faceted but instead have a nearly sinusoidal profile. The second additional term that appears in the EOM when there is a miscut can be thought of as a source of nonlinear dispersion. When its coefficient (κ) is sufficiently large, this term can disrupt the order produced by strong linear dispersion. However, by adjusting the angle of incidence θ, the ratio κ/γ can be made small. Ion bombardment will then produce highly ordered ripples with a nearly sinusoidal profile on the GaAs surface.

This paper is organized as follows: We present a derivation of the EOM in Sec. II. In Sec. III, we recast the EOM in dimensionless form and consider the behavior of its solutions at early times, before the effect of the nonlinear terms becomes appreciable. Previous results on the behavior of the surface when the ion beam is normally incident and there is no miscut are briefly summarized in Sec. IV. For a certain special case, the EOM is equivalent to a generalization of the one-dimensional Cahn-Hillard equation to two dimensions, as we show in Sec. V. As a consequence, the surface can exhibit nucleation and growth of facets as well as spinodal decomposition. The case of strong linear dispersion is studied in Sec. VI using an expansion in powers of γ^{-1} and simulations. We place our results in context in Sec. VII and conclude in Sec. VIII.

II. EQUATION OF MOTION

Consider the planar surface of a single crystal of GaAs. We take the surface to be the (001) plane or the (001) plane with a small miscut along the [110] direction. We place the origin on the surface of the sample and orient the z axis so that the sample occupies the region $z \leqslant 0$. In addition, we orient the x axis so that it is parallel to the surface projection of the [110] direction. The normal to the (001) crystal planes is $-\hat{\boldsymbol{x}} \sin\psi + \hat{\boldsymbol{z}} \cos\psi$, where ψ is the miscut angle.

We now perturb the sample surface slightly and bombard it with a broad noble gas ion beam. The energy of the incident ions will be taken to be below the sputtering threshold so that sputtering is negligible. The incident ion flux is $\boldsymbol{J} = -J\hat{\boldsymbol{e}}$, where $\hat{\boldsymbol{e}} \equiv -\hat{\boldsymbol{x}} \sin\theta + \hat{\boldsymbol{z}} \cos\theta$ and θ is the the angle of incidence, i.e., the angle between the global vertical and the incident beam. The projected ion direction lies along the x direction. We will take θ to be either zero or small.

We will employ a continuum description of the surface dynamics in which the position of an arbitrary point $\boldsymbol{r}$ on the film's surface is given by $\boldsymbol{r} = x\hat{\boldsymbol{x}} + y\hat{\boldsymbol{y}} + u(x, y, t)\hat{\boldsymbol{z}}$, where $u(x, y, t)$ is the height of the point above the x-y plane at time t. The surface height u is obtained by coarse-graining the detailed microscopic surface configuration and is assumed to be a smoothly varying function of its arguments x, y, and t. We assume that no overhangs are initially present and that none form as the film grows, so that $u(x, y, t)$ is a single-valued function of x and y for all times t.

Well above the recrystallization temperature, the damage done to the crystal structure by the ion impacts is rapidly annealed away, and the sample remains essentially crystalline. Pattern formation on the surface of materials that remain crystalline during ion bombardment is strongly influenced by the Ehrlich-Schwoebel (ES) barrier [26–29]. The ES barrier makes the attachment of a surface vacancy more likely at a descending step on a crystal surface than at an ascending step. It therefore produces an effective uphill atomic current on the crystal's surface and tends to destabilize an initially flat surface. This current is typically anisotropic, which is a manifestation of the anisotropy of the underlying crystal lattice. For T well below T_R, on the other hand, the damage quickly accumulates as time passes and an amorphous layer develops at the surface of the solid. Momentum transfer from the incident ions to atoms near the surface of the solid leads to mass redistribution (MR) which has a stabilizing influence for normal-incidence ion bombardment [30–32]. Between the low- and high-temperature extremes, the subsurface damage varies continuously with temperature, and therefore so does the surface atomic current. The stabilizing effect of MR is stronger than the destabilizing influence of the ES barrier for $T < T_{c,0}$ and $\theta = \psi = 0$ and, as a consequence, the surface remains flat. Conversely, for $T > T_{c,0}$ and $\theta = \psi = 0$, the ES effect dominates MR, the surface is unstable, and ripples with their wave vector along the x axis form on the surface. The surface becomes unstable for T greater than the critical temperature $T_c(\theta, \psi)$ when θ and ψ are nonzero. Clearly, $T_c(-\theta, -\psi) = T_c(\theta, \psi)$ and $T_c(0, 0) = T_{c,0}$.

Ions are implanted in the low-energy regime. However, the noble gas ions penetrate only a few nanometers into the solid, are highly mobile, and usually desorb when they reach the solid surface [33]. Ion implantation can therefore be safely neglected.

When sputtering and implantation are neglected, the mass of the solid is conserved. This makes the low-energy limit fundamentally different than the higher energy regime in which sputtering is significant. In addition, while curvature-dependent sputtering and ion implantation can contribute to the surface instability in the higher energy regime [34–36], they do not do so in the low-energy regime.

The ratio of gallium atoms to arsenic atoms remains one-to-one during the irradiation because there is no sputtering. In principle, MR could affect the gallium and arsenic atoms differently and so change the composition locally [4,5]. However, differential mass redistribution has been found to be negligible for bombardment of GaSb with 250 eV Ar ions [37,38]. Because the mass difference between Ga and As is considerably smaller than the mass difference between Ga and Sb, we will assume that differential mass redistribution

is also negligible for GaAs. Furthermore, in the absence of any information to the contrary, we will take the difference between the surface currents of Ga and As due to the ES effect to be small enough that it can be neglected. The composition then remains stoichiometric throughout the sample, which minimizes the chemical free energy of the solid. Similarly, Ou *et al.* [14] assumed that the composition remains stoichiometric throughout the solid in developing their phenomenological theory.

Let $\boldsymbol{j} = j_x\hat{\boldsymbol{x}} + j_y\hat{\boldsymbol{y}} + j_z\hat{\boldsymbol{z}}$ be the atomic current on the surface of the solid. The current $\boldsymbol{j}$, which is everywhere tangent to the solid surface, includes contributions from the ES effect and thermally activated surface diffusion in the high-temperature regime, while in the low-temperature regime, MR and ion-induced surface viscous flow [39] could contribute to $\boldsymbol{j}$. Because mass is conserved, the equation of motion for the surface is the continuity equation

$$u_t = -\Omega(\partial_x j_x + \partial_y j_y), \tag{1}$$

where Ω is the atomic volume. The surface current $\boldsymbol{j}$ depends on the angle of ion incidence θ and the miscut angle ψ. Its value at time t also depends in principle on the form of the entire surface at that time. In other words, for $i = x$ and y,

$$j_i = j_i(\theta, \psi, u_x, u_y, u_{xx}, u_{xy}, u_{yy}, \ldots), \tag{2}$$

where the subscripts on u denote partial derivatives. Hence,

$$\Omega^{-1}u_t = -\partial_x j_x(\theta, \psi, u_x, u_y, \ldots) - \partial_y j_y(\theta, \psi, u_x, u_y, \ldots). \tag{3}$$

$\boldsymbol{j}$ also depends on the sample temperature T, as we have already noted. However, we have not included T in the list of arguments of $\boldsymbol{j}$ for the sake of notational simplicity.

Equation (3) completely specifies the dynamics of the surface but, in general, it is exceedingly complicated nonlinear partial differential equation. In addition, how j_x and j_y depend on the temperature T, the angle of incidence θ, the miscut angle ψ and all of the surface derivatives u_x, u_y, u_{xx}, u_{xy}, u_{yy}, etc. is not known for any noble gas ion species or energy. Fortunately, the surface dynamics become much simpler close to the critical temperature $T_{c,0}$ and for small values of θ and ψ. We set $\epsilon \equiv |T - T_{c,0}|^{1/2}$, where ϵ is small and positive. Because we wish to consider small angles of incidence θ and miscut angles ψ, we take θ and ψ to be of order ϵ and put

$$\theta = \rho_\theta \epsilon \tag{4}$$

and

$$\psi = \rho_\psi \epsilon, \tag{5}$$

where ρ_θ and ρ_ψ are constants of proportionality. (The special case in which the ion beam is normally incident and there is no miscut is obtained by setting $\rho_\theta = \rho_\psi = 0$.) We seek solutions to Eq. (3) of the form

$$u(x, y, t) = U(X, Y, \tau), \tag{6}$$

where

$$X \equiv \epsilon x, \quad Y \equiv \epsilon^2 y, \quad \text{and} \quad \tau \equiv \epsilon^4 t. \tag{7}$$

X, Y, and τ are the so-called "slow" variables and x, y and t are the corresponding "fast" variables. Heuristically speaking, Eqs. (6) and (7) say that for T close to the threshold temperature $T_{c,0}$ and for small θ and ψ, the height of the surface disturbance varies slowly in space and time. In addition, the spatial variation in the y direction is more gradual than in the x direction because ripples with their wave vector pointing in the x direction develop for $T > T_c(\theta, \psi)$. An *a posteriori* justification for adopting the scaling ansatz given by Eqs. (4)–(7) will be obtained once we have arrived at an EOM that is well-behaved in the $\epsilon \to 0$ limit.

Using the scaling given by Eqs. (6) and (7) in Eq. (3), we obtain

$$\begin{aligned} -\Omega^{-1}\epsilon^4 U_\tau = {} & \epsilon \partial_X j_x(\theta, \psi, \epsilon U_X, \epsilon^2 U_Y, \epsilon^2 U_{XX}, \epsilon^3 U_{XY}, \epsilon^4 U_{YY}, \ldots) \\ & + \epsilon^2 \partial_Y j_y(\theta, \psi, \epsilon U_X, \epsilon^2 U_Y, \epsilon^2 U_{XX}, \epsilon^3 U_{XY}, \epsilon^4 U_{YY}, \ldots). \end{aligned} \tag{8}$$

Let $j_{x,n}$ denote the derivative of $j_x(\theta, \psi, u_x, u_y, u_{xx}, u_{xy}, u_{yy}, \ldots)$ with respect to its nth argument evaluated for $\theta = \psi = u_x = u_y = u_{xx} = u_{xy} = u_{yy} = \ldots = 0$. We define $j_{y,n}$ in an analogous fashion. The definition of quantities like $j_{x,n,m}$ and $j_{y,n,m}$ should now be apparent. We expand Eq. (8) in powers of ϵ and retain terms up to fourth order in ϵ. The EOM must be invariant under the transformation $Y \to -Y$ and so the coefficients of terms that do not have this invariance must have coefficients equal to zero. In addition, the EOM must be invariant under the transformation $X \to -X$, $\theta \to -\theta$, and $\psi \to -\psi$. We obtain

$$\begin{aligned} -\Omega^{-1}\epsilon^4 U_\tau = {} & \epsilon^2\big(j_{x,3} + \tfrac{1}{2}j_{x,1,1,3}\theta^2 + j_{x,1,2,3}\theta\psi + \tfrac{1}{2}j_{x,2,2,3}\psi^2\big)U_{XX} + \epsilon^4 j_{x,8}U_{XXXX} + \epsilon^4 j_{y,4}U_{YY} \\ & + \tfrac{1}{6}\epsilon^4 j_{x,3,3,3}\partial_X U_X^3 + \tfrac{1}{2}\epsilon^4 j_{x,3,5}\partial_X^2 U_X^2 + \epsilon^3(j_{x,1,5}\theta + j_{x,2,5}\psi)U_{XXX} + \tfrac{1}{2}\epsilon^3(j_{x,1,3,3}\theta + j_{x,2,3,3}\psi)\partial_X U_X^2. \end{aligned} \tag{9}$$

For normal-incidence bombardment of a surface with no miscut, the surface is stable for $T < T_{c,0}$ and is unstable for $T > T_{c,0}$. This means that $j_{x,3}$ is negative for $T < T_{c,0}$ and is positive for $T > T_{c,0}$. For small enough values of $T - T_{c,0}$, we can make the approximation $j_{x,3} = A_1(T - T_{c,0})$, where A_1 is a positive constant. Hence, close to the critical temperature, $j_{x,3} = sA_1\epsilon^2$, where s is the sign of $T - T_{c,0}$. Recalling that we set $\theta = \rho_\theta\epsilon$ and $\psi = \rho_\psi\epsilon$, Eq. (9) becomes

$$\begin{aligned} -\Omega^{-1}U_\tau = {} & \big(sA_1 + \tfrac{1}{2}j_{x,1,1,3}\rho_\theta^2 + j_{x,1,2,3}\rho_\theta\rho_\psi + \tfrac{1}{2}j_{x,2,2,3}\rho_\psi^2\big)U_{XX} + j_{x,8}U_{XXXX} + j_{y,4}U_{YY} \\ & + \tfrac{1}{6}j_{x,3,3,3}\partial_X U_X^3 + \tfrac{1}{2}j_{x,3,5}\partial_X^2 U_X^2 + (j_{x,1,5}\rho_\theta + j_{x,2,5}\rho_\psi)U_{XXX} + \tfrac{1}{2}(j_{x,1,3,3}\rho_\theta + j_{x,2,3,3}\rho_\psi)\partial_X U_X^2. \end{aligned} \tag{10}$$

Notice that ϵ does not appear in Eq. (10), and so the scaling we adopted does indeed result in an EOM that is well defined in the $\epsilon \to 0$ limit. Equation (10) is invariant under the transformation $Y \to -Y$. In addition, for normal-incidence bombardment of a surface with no miscut, $\rho_\theta = \rho_\psi = 0$ and then Eq. (10) is also invariant under the transformation $X \to -X$.

We must have $j_{x,8} > 0$, since otherwise arbitrarily short wavelengths are linearly unstable and the continuum description breaks down. In addition, $j_{x,3,3,3}$ cannot be positive since if it were, the slope of the surface would grow without bound. Finally, $j_{y,4}$ must be negative because the flat surface is stable for $T < T_{c,0}$ and $\theta = \psi = 0$. Equation (10) becomes

$$U_\tau = -AU_{XX} - BU_{XXXX} + DU_{YY} + \alpha \partial_X U_X^3 + \beta \partial_X^2 U_X^2 + \mu U_{XXX} + \nu \partial_X U_X^2, \tag{11}$$

where

$$A \equiv \Omega\big(sA_1 + \tfrac{1}{2} j_{x,1,1,3}\rho_\theta^2 + j_{x,1,2,3}\rho_\theta\rho_\psi + \tfrac{1}{2} j_{x,2,2,3}\rho_\psi^2\big), \tag{12}$$

$$B \equiv \Omega j_{x,8},\ D \equiv \Omega|j_{y,4}|,\ \alpha \equiv \Omega|j_{x,3,3,3}|/6,\ \beta \equiv -\Omega j_{x,3,5}/2,$$
$$\mu \equiv -\Omega(j_{x,1,5}\rho_\theta + j_{x,2,5}\rho_\psi), \tag{13}$$

and

$$\nu \equiv -\tfrac{1}{2}\Omega(j_{x,1,3,3}\rho_\theta + j_{x,2,3,3}\rho_\psi). \tag{14}$$

The coefficients B and D in Eq. (11) are positive whereas α is nonnegative. (As we shall see shortly, α must in fact be positive.) In addition, by replacing U by $-U$ if necessary, we can arrange for β to be nonnegative. We can also arrange for μ to be nonnegative by replacing X by $-X$ if necessary.

When there is no miscut and the ion beam is normally incident, $\mu = \nu = 0$ and Eq. (11) with $s = +1$ reduces to the EOM that Ou *et al.* used to model the dynamics of the (001) surface of GaAs when it is subjected to normal-incidence bombardment at temperatures $T > T_{c,0}$ [14]. Ou and coworkers arrived at this EOM using phenomenological arguments, but we have shown rigorously that it is valid close to the critical temperature.

Thermally activated surface diffusion and/or ion-induced surface viscous flow lead to the presence of the term $-BU_{XXXX}$ in Eq. (11) [39,40]. The terms proportional to U_{XX}, U_{YY}, $\partial_X U_X^2$, and $\partial_X U_X^3$ all result from the dependence of the surface current $\boldsymbol{j}$ on the surface gradient ∇u. This dependence stems from the ES effect and ion-induced MR. The term $\alpha\partial_X U_X^3$ in particular is familiar from the theory of the mounding instability that can occur during molecular beam epitaxy and can lead to the formation of a faceted surface [29]. Because the GaAs surface facets for $T > T_{c,0}$ and $\theta = \psi = 0$, the coefficient α cannot be zero. The term $\beta\partial_X^2 u_X^2$, on the other hand, is the so-called conserved Kuramoto-Sivashinsky (CKS) nonlinearity. Although it was first encountered in the theory of molecular beam epitaxy [29,41], this term is also believed to play a role in the dynamics of ion-bombarded surfaces [42,43]. The CKS nonlinearity tends to produce coarsening of the surface patterns, i.e., the characteristic lateral and vertical length scales tend to increase with time. If there is no miscut, the beam is normally incident and β is nonzero, this term breaks the $U \to -U$ symmetry that would otherwise be present. Since there is vacuum above the surface and solid below, there is no reason that such a symmetry should exist.

The final two terms on the right-hand side of Eq. (11) break the $X \to -X$ symmetry and appear only when θ and/or ψ is nonzero. The term proportional to U_{XXX} arises because the surface current due to MR depends on the curvature of the surface, as shown by molecular dynamics simulations of bombardment of silicon with a 1 keV argon ion beam [33]. This term produces linear dispersion, i.e., the propagation velocity of low amplitude surface ripples depends on their wavelength. A term proportional to U_{XXX} also appears in the EOM that describes the step bunching instability of a vicinal surface [44] and so its appearance in Eq. (11) when there is a miscut is perhaps not surprising. The term proportional to $\partial_X U_X^2$ appears in Eq. (11) because the angles that the facets make with the X-Y plane depend on the angle of incidence θ and the miscut angle ψ [14,45]. This term can change the ripple velocity as its amplitude grows [46] and will therefore be referred to as nonlinearly dispersive.

How slowly must the height of the surface disturbance u vary with x for Eq. (11) to be valid? Let a_0 be the characteristic size of a collision cascade, or, equivalently, the characteristic lateral length scale of the crater that the impact of a single ion produces on the GaAs surface. The characteristic lateral length scale (or length scales) of the surface ripple must be large compared to a_0 for Eq. (11) to be a good approximation. If the surface disturbance is sinusoidal, then it has a single characteristic lateral length scale—its wavelength. However, if the surface disturbance is periodic but the characteristic lateral length scale of the crests l_+ differs from the characteristic lateral length scale of the troughs l_-, then both l_+ and l_- must be large compared to a_0 for Eq. (11) to apply. This possibility is not academic—in general, l_+ and l_- differ [47].

Equation (11) is

$$u_t = \partial_x\big(au_x + bu_x^2 + \alpha u_x^3\big) - Bu_{xxxx} + Du_{yy} + \beta\partial_x^2 u_x^2 + cu_{xxx} \tag{15}$$

when written in terms of the original variables. Here

$$a \equiv -\Omega\big[A_1(T - T_{c,0}) + \tfrac{1}{2} j_{x,1,1,3}\theta^2 + j_{x,1,2,3}\theta\psi + \tfrac{1}{2} j_{x,2,2,3}\psi^2\big], \tag{16}$$

$$b \equiv -\Omega(j_{x,1,3,3}\theta + j_{x,2,3,3}\psi)/2, \tag{17}$$

and

$$c \equiv -\Omega(j_{x,1,5}\theta + j_{x,2,5}\psi). \tag{18}$$

Recall that the surface is stable for $T < T_c(\theta, \psi)$ and is unstable for $T > T_c(\theta, \psi)$. Therefore, a is positive for $T < T_c(\theta, \psi)$ and is negative for $T > T_c(\theta, \psi)$. It follows that

$$T_c(\theta, \psi) = T_{c,0} - \frac{1}{2A_1}(j_{x,1,1,3}\theta^2 + 2j_{x,1,2,3}\theta\psi + j_{x,2,2,3}\psi^2). \tag{19}$$

$T_c(-\theta, -\psi) = T_c(\theta, \psi)$ and $T_c(0, 0) = T_{c,0}$, as we have already observed. In addition, combining Eqs. (16) and (19), we obtain

$$a = -\Omega A_1[T - T_c(\theta, \phi)]. \tag{20}$$

III. PRELIMINARY CONSIDERATIONS

Consider the behavior of solutions to the EOM (11) for $T > T_c$, so that $A > 0$ and the surface is unstable. We introduce the dimensionless quantities

$$\tilde{x} \equiv \left(\frac{A}{B}\right)^{1/2} X, \quad \tilde{y} \equiv \frac{A}{(DB)^{1/2}} Y,$$
$$\tilde{t} \equiv \frac{A^2}{B}\tau, \quad \text{and} \quad \tilde{u} \equiv \left(\frac{\alpha}{B}\right)^{1/2} U. \tag{21}$$

Making these substitutions in Eq. (11) and dropping the tildes yields

$$u_t = -u_{xx} + u_{yy} - u_{xxxx} + \partial_x u_x^3 + r\partial_x^2 u_x^2 + \gamma u_{xxx} + \kappa \partial_x u_x^2, \tag{22}$$

where $r \equiv \beta(\alpha B)^{-1/2} \geqslant 0$, $\gamma \equiv \mu(AB)^{-1/2} \geqslant 0$, and $\kappa \equiv \nu(AB)^{-1/2}$ are dimensionless parameters. If the surface height u does not depend on the transverse coordinate y, then Eq. (22) reduces to

$$u_t = -u_{xx} - u_{xxxx} + \partial_x u_x^3 + r\partial_x^2 u_x^2 + \gamma u_{xxx} + \kappa \partial_x u_x^2, \tag{23}$$

which we will refer to as the 1D EOM.

Because the surface is nominally flat at time $t = 0$, Eq. (22) can be linearized at early times. The linearized EOM has sinusoidal solutions of the form

$$u(x, y, t) = \mathrm{Re}\,[u_0 \exp(i\boldsymbol{k} \cdot \boldsymbol{x} + \sigma t)], \tag{24}$$

where u_0 is an arbitrary complex constant, $\boldsymbol{x} \equiv x\hat{\boldsymbol{x}} + y\hat{\boldsymbol{y}}$, $\boldsymbol{k} \equiv k_x\hat{\boldsymbol{x}} + k_y\hat{\boldsymbol{y}}$ is the wave vector, and

$$\sigma = \sigma(\boldsymbol{k}) = k_x^2 - k_x^4 - k_y^2 - i\gamma k_x^3. \tag{25}$$

The amplitude of this sinusoidal ripple grows exponentially in time with the rate $\mathrm{Re}\,\sigma(\boldsymbol{k}) = k_x^2 - k_x^4 - k_y^2$. [The amplitude decays exponentially if $\mathrm{Re}\,\sigma(\boldsymbol{k})$ is negative.] In addition, the ripple propagates with the velocity $-\mathrm{Im}\,\sigma(\boldsymbol{k})/k = \gamma k_x^3/k$ in the direction of its wave vector. If γ is nonzero, then the propagation is dispersive because the velocity of propagation depends on the wavelength. $\mathrm{Re}\,\sigma(\boldsymbol{k})$ is maximized for $k_x = 1/\sqrt{2}$ and $k_y = 0$. It follows that ripples with wavelength $2\sqrt{2}\pi$ and with their wave vector along the x direction emerge shortly after the irradiation begins. These ripples propagate in the x direction with velocity $\gamma/2$.

The full nonlinear EOM (22) depends on three dimensionless parameters, r, γ, and κ. The parameters r, γ, and κ are measures of the strength of the CKS nonlinearity, linear dispersion and nonlinear dispersion, respectively. For the sake of simplicity, we will begin by studying the behavior of Eq. (22) for the special cases in which only r is nonzero (Sec. IV) and in which only κ is nonzero (Sec. V). We will then move on to study the case in which γ is nonzero in Sec. VI. In that section, we will also study cases in which either r or κ is nonzero. The distinctive features of the dynamics will be highlighted in each these of three sections.

IV. NORMAL-INCIDENCE BOMBARDMENT OF A SAMPLE WITH NO MISCUT

If there is no miscut and the ion beam is normally incident on the sample surface, then $\gamma = \kappa = 0$ in the EOM (22) but r is in general nonzero. This is the partial differential equation (PDE) Ou *et al.* used to model normal-incidence bombardment of the (001) surface of GaAs above the recrystallization temperature [14]. It is also the EOM for the surface of a growing thin amorphous film that is deposited by two diametrically opposed atomic beams that are obliquely incident on a planar substrate and has been studied extensively in that context [47]. Here we will simply summarize the results of that investigation, rephrasing them in the context of the current problem.

At early times, the ripples that form on the surface are rounded and roughly sinusoidal in form, but as time passes, they coarsen and become more faceted. At long times, the ripples become highly ordered in the transverse direction and few dislocations remain. The ripple wavelength and amplitude vary in the longitudinal direction, however, and so the ripples are not perfectly ordered.

The selected gradients are $\nabla u = \pm\hat{\boldsymbol{x}}$. Thus, surprisingly, the selected slope does not depend on the coefficient r of the CKS nonlinearity. The ripple crests and troughs are both rounded, but for $r > 0$, the troughs are more rounded than the crests. The surface ripples therefore display vertical asymmetry, i.e., the appearance of the ripples changes if they are reflected about the x-y plane. As r is increased, the rounding of the troughs becomes more pronounced, while the crests become progressively sharper. At the same time, the facets become smaller. All of these aspects of the dynamics are discussed in detail in Ref. [47] and are illustrated there by quite a number of simulations.

V. NUCLEATION AND GROWTH OF FACETS AND SPINODAL DECOMPOSITION

We now move on to the case in which κ is nonzero and the linearly dispersive and CKS terms do not appear in Eq. (22), i.e., γ and r both vanish. In this case, it is best to study the EOM written in terms of the original, unscaled variables, Eq. (15). The reason for this is that we will want to study the behavior of the surface for both positive and negative values of A, but we limited ourselves to the case in which $A > 0$ in deriving Eq. (22). In the special case we are currently considering, $\beta = c = 0$ in Eq. (15), and we are interested in the effect of varying the parameter b. This parameter is nonzero only if there is a miscut.

Differentiating Eq. (15) with respect to x, setting $\beta = c = 0$ and defining $\phi \equiv u_x$, we obtain

$$\phi_t = \partial_x^2(a\phi + b\phi^2 + \alpha\phi^3 - B\phi_{xx}) + D\phi_{yy}. \tag{26}$$

If the surface height u does not depend on the transverse coordinate y, then $\phi_y = 0$ and Eq. (26) reduces to the one-dimensional Cahn-Hilliard (CH) equation. Equation (26) is therefore an anisotropic generalization of the one-dimensional CH equation to two dimensions (2D). Variations of the surface height in the transverse direction tend to be smoothed out in the course of time as a result of presence of the term $D\phi_{yy}$ in Eq. (26), and so the solutions of this equation increasingly resemble solutions to the one-dimensional (1D) CH equation as time passes. Because the behavior of solutions to the 1D CH equation is well known [48], our discussion of the behavior of Eq. (15) with $\beta = c = 0$ will be brief.

We study the behavior of the solutions to Eq. (15) with $\beta = c = 0$ in the domain in which $0 \leqslant x \leqslant L$ and $0 \leqslant y \leqslant L$ and apply periodic boundary conditions. We introduce the effective free energy

$$F \equiv \int_0^L \int_0^L \left[\frac{1}{2}Bu_{xx}^2 + f(u_x, u_y)\right] dxdy, \tag{27}$$

where

$$f(u_x, u_y) \equiv \frac{a^2}{4\alpha} + \frac{1}{2}au_x^2 + \frac{1}{3}bu_x^3 + \frac{1}{4}\alpha u_x^4 + \frac{1}{2}Du_y^2 \tag{28}$$

will be referred to as the effective potential. Equation (15) with $\beta = c = 0$ can be written

$$u_t = -\frac{\delta F}{\delta u}, \tag{29}$$

where $\delta F/\delta u$ denotes the variational derivative of F with respect to the surface height u. Equation (29) implies that $dF/dt \leqslant 0$, i.e., the effective free energy can never increase. The dynamics therefore tends to minimize the value of F. This greatly facilitates the analysis.

When $\theta = \psi = 0$ and $T > T_{c,0}$, a is negative and $b = 0$. In this case, the behavior is analogous to the behavior of the 1D CH equation for a critical quench and the surface undergoes spinodal decomposition [48]. The effective potential f has minima at $(u_x, u_y) = (\pm(|a|/\alpha)^{1/2}, 0)$. Therefore, the surface will tend toward a state in which most of the surface has a gradient ∇u nearly equal to $\pm(|a|/\alpha)^{1/2}\hat{\mathbf{x}}$, i.e., the surface will facet. The facets have an effective free energy equal to zero. Adjacent facets are separated by "edges" which have a positive free energy per unit length. ∇u changes rapidly but not discontinuously as an edge is traversed. As some facets contract and disappear and others grow, the pattern coarsens, the total length of the edges declines, and the effective free energy decreases.

The facet slope that is selected is $(|a|/\alpha)^{1/2} = (\Omega A_1/\alpha)^{1/2}(T - T_{c,0})^{1/2}$ and will be referred to as the selected slope for the sake of brevity. It increases with the temperature and decreases with the coefficient α of the cubic ES nonlinearity.

When θ and/or ψ is nonzero, b is nonzero and the effective potential $f(u_x, u_y)$ is asymmetric, i.e., it is not invariant under the transformation $u_x \to -u_x$. In this case, the behavior is analogous to the behavior of the 1D CH equation for an off-critical quench [48]. For $a > a_c = 2b^2/(9\alpha)$, the state $u_x = u_y = 0$ is stable. Thus, for temperatures T sufficiently far below T_c, the surface smooths. In the coexistence region $0 < a < a_c$, on the other hand, there is a local minimum in the potential $f(u_x, u_y)$ at $u_x = u_y = 0$. The global minimum in the potential is at $u_x = \phi_* \equiv -(b + \sqrt{b^2 - 4a\alpha})/2\alpha < 0$ and $u_y = 0$. The flat state $u_x = u_y = 0$ is therefore metastable. Noise in the initial condition or shot noise in the ion beam could lead to nucleation and growth of regions with u_x values ϕ_1 and ϕ_2 which satisfy $\phi_* < \phi_1 < 0$ and $\phi_2 > 0$. The value of u_y in these regions is zero. The surface slope varies smoothly in interfacial regions between adjacent regions in which the slope is very nearly constant. The width of these interfacial regions depends on B. The precise values of the slopes ϕ_1 and ϕ_2 can be determined using the requirement that the line joining the points $(\phi_1, f(\phi_1))$ and $(\phi_2, f(\phi_2))$ must be tangent to the curve $f = f(\phi)$ at these two points. Finally, for $a \leqslant 0$, the flat state $u_x = u_y = 0$ is unstable and spinodal decomposition occurs. Once again, regions in which $u_y = 0$ and u_x is nearly equal to one of two selected values develop at long times and are separated by interfacial regions in which the slope varies smoothly.

The behavior for a case in which $0 < a < a_c$ and b is nonzero is illustrated by Fig. 1. In this simulation, a small nucleation site was introduced at time $t = 0$. To create this nucleus, we first introduced a small region with the selected slopes on a surface. This region had discontinuities in height at its edges, and so the surface was smoothed by averaging the height at each grid point with the heights of its nearest neighbors, giving us the initial condition seen in Fig. 1(a). As time progressed, the area of the region in which u_x is nearly equal to one of the selected values ϕ_1 and ϕ_2 increased, as shown in Figs. 1(b) and 1(c). Ultimately, this region expanded to fill the entire domain (not shown).

VI. HIGHLY ORDERED, NEARLY SINUSOIDAL RIPPLES

It would be natural at this point to study the special case of Eq. (22) in which $r = \kappa = 0$ and the coefficient of the linearly dispersive term γ is nonzero. (Note that for γ to be nonzero, θ and ψ cannot both be zero.) As we shall see, in this case, highly ordered, nearly sinusoidal ripples form if γ is sufficiently large. In fact, even if r or κ is nonzero, highly ordered, nearly sinusoidal ripples emerge if γ is large enough. We will therefore also consider cases in which r or κ are nonzero in this section.

It is important to note that it is possible to make γ large relative to r and κ in an experiment. To see this, we begin by noting that

$$\gamma = -\frac{\Omega(j_{x,1,5}\theta + j_{x,2,5}\psi)}{\{\Omega A_1 B[T - T_c(\theta, \psi)]\}^{1/2}}. \tag{30}$$

γ can therefore be made as large as desired by choosing T to be close to $T_c(\theta, \psi)$ but greater than it. In addition,

$$2\frac{\kappa}{\gamma} = \frac{j_{x,1,3,3}\theta + j_{x,2,3,3}\psi}{j_{x,1,5}\theta + j_{x,2,5}\psi}. \tag{31}$$

Suppose the miscut angle ψ is fixed. Equation (31) shows that it is possible to arrange for κ/γ to be zero by an appropriate choice of the angle of incidence θ. In an actual experiment, κ/γ could not be made equal to zero precisely but it certainly could be made small, and so the requirement $\kappa \ll \gamma$ can be satisfied by adjusting the angle of incidence. Finally, r does not depend on θ or ψ and depends only weakly on the temperature T. This means that we can also arrange to have $\gamma \gg r$ by choosing $T - T_c(\theta, \psi)$ to be small and positive.

Because we are especially interested in finding means to produce highly ordered ripples, the emphasis in this section will be on the behavior for large γ. As we shall see, it is possible to make analytical progress on Eq. (22) in that limit.

A. Perturbation expansion

To gain insight into the form that the surface takes at long times when γ is large, we will find approximate solutions to the 2D EOM (22) by carrying out a perturbation expansion in

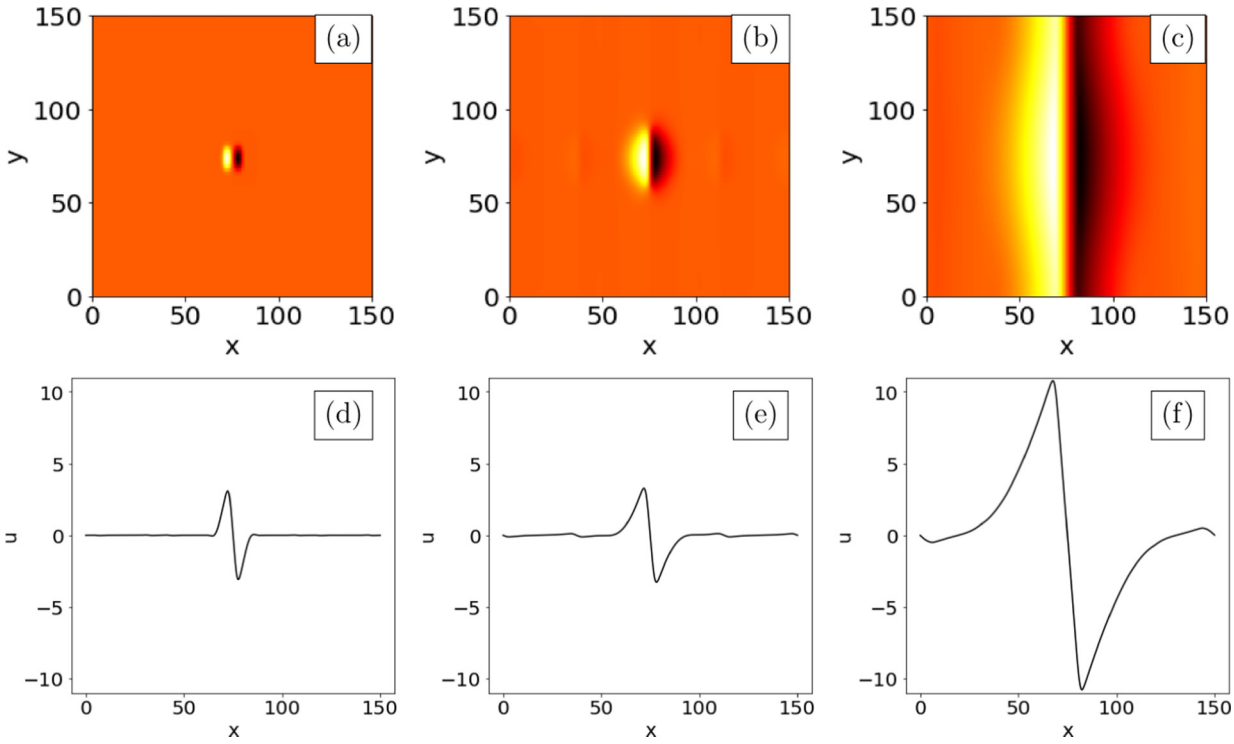

FIG. 1. Top row: Plots of the surface height u at (a) $t = 0$, (b) $t = 50$, and (c) $t = 500$, obtained from integration of Eq. (15) with the following parameter values: $a = 0.1$, $\alpha = 1$, $B = 1$, $D = 1$, $\beta = 0$, $c = 0$, and $b = 2$. Bottom row: Cuts of the surface along the horizontal axis at $y = 75$, (d), (e), and (f), at the corresponding times. The domain size is 150×150.

powers of the small parameter $\varepsilon \equiv 1/\gamma$. ($\varepsilon$ is not to be confused with $\epsilon \equiv |T - T_{c,0}|^{1/2}$.) In particular, we seek solutions of the form $u = u(\xi)$, where $\xi \equiv x - vt$. These traveling wave solutions are independent of time in the frame of reference that propagates in the x direction with the wave velocity v. We obtain

$$-vu_\xi = -u_{\xi\xi} - u_{\xi\xi\xi\xi} + \partial_\xi u_\xi^3 + \gamma u_{\xi\xi\xi} + r\partial_\xi^2 u_\xi^2 + \kappa \partial_\xi u_\xi^2. \tag{32}$$

We integrate this equation once with respect to ξ and eliminate the resulting constant of integration C by setting $\tilde{u} = u - C/v$ and then dropping the tildes. Equation (32) becomes

$$u_{\xi\xi} + \omega u + \varepsilon\left(-u_\xi - u_{\xi\xi\xi} + u_\xi^3 + r\partial_\xi u_\xi^2 + \kappa u_\xi^2\right) = 0, \tag{33}$$

where $\omega \equiv \varepsilon v$.

We now set $u = u_0 + u_1 + \cdots$ and $\omega = \omega_0 + \omega_1 + \cdots$, where u_n and ω_n are of order ε^n. Working to order ε^0, we obtain

$$u_{0\xi\xi} + k^2 u_0 = 0, \tag{34}$$

where $k \equiv \sqrt{\omega_0}$. This equation has the solution

$$u_0 = A_0 \cos(k\xi), \tag{35}$$

where we have chosen a phase and the amplitude A_0 is a constant. The equation we obtain by retaining terms up to order ε^1 is

$$\mathcal{L}u_1 = q, \tag{36}$$

where $\mathcal{L} \equiv \partial_\xi^2 + k^2$ is a differential operator and

$$q \equiv -\omega_1 u_0 + \varepsilon\left(u_{0\xi} + u_{0\xi\xi\xi} - u_{0\xi}^3 - r\partial_\xi u_{0\xi}^2 - \kappa u_{0\xi}^2\right). \tag{37}$$

Inserting our result Eq. (35) into Eq. (37), we find that

$$\begin{aligned} q = {} & -\omega_1 A_0 \cos(k\xi) + \varepsilon k A_0 \left(-1 + k^2 + \frac{3}{4}k^2 A_0^2\right) \sin(k\xi) \\ & - \frac{1}{2}\varepsilon\kappa k^2 A_0^2 + \frac{1}{2}\varepsilon\kappa k^2 A_0^2 \cos(2k\xi) - \varepsilon r k^3 A_0^2 \sin(2k\xi) \\ & - \frac{1}{4}\varepsilon k^3 A_0^3 \sin(3k\xi). \end{aligned} \tag{38}$$

The operator $\mathcal{L}$ is self-adjoint, and so according to the Fredholm alternative, Eq. (36) has a solution if and only if q is orthogonal to the kernel of $\mathcal{L}$. $\sin(k\xi)$ and $\cos(k\xi)$ are in the kernel of $\mathcal{L}$, and so the coefficients of $\sin(k\xi)$ and $\cos(k\xi)$ in q must be zero. As a consequence,

$$k = \left(1 + \tfrac{3}{4}A_0^2\right)^{-1/2} \tag{39}$$

and

$$\omega_1 = 0. \tag{40}$$

Recalling that $\omega = \varepsilon v = \omega_0 + \omega_1 + \ldots$ and $\omega_0 = k^2$, we obtain

$$v = \gamma\left(1 + \tfrac{3}{4}A_0^2\right)^{-1} + O(\varepsilon). \tag{41}$$

Making use of Eqs. (39) and (40), we see that Eq. (36) reduces to

$$\begin{aligned} \mathcal{L}u_1 = {} & -\tfrac{1}{2}\varepsilon\kappa k^2 A_0^2 + \tfrac{1}{2}\varepsilon\kappa k^2 A_0^2 \cos(2k\xi) - \varepsilon r k^3 A_0^2 \sin(2k\xi) \\ & - \tfrac{1}{4}\varepsilon k^3 A_0^3 \sin(3k\xi). \end{aligned} \tag{42}$$

We set

$$u_1 = B_0 + B_1 \cos(2k\xi) + B_2 \sin(2k\xi) + B_3 \sin(3k\xi) \tag{43}$$

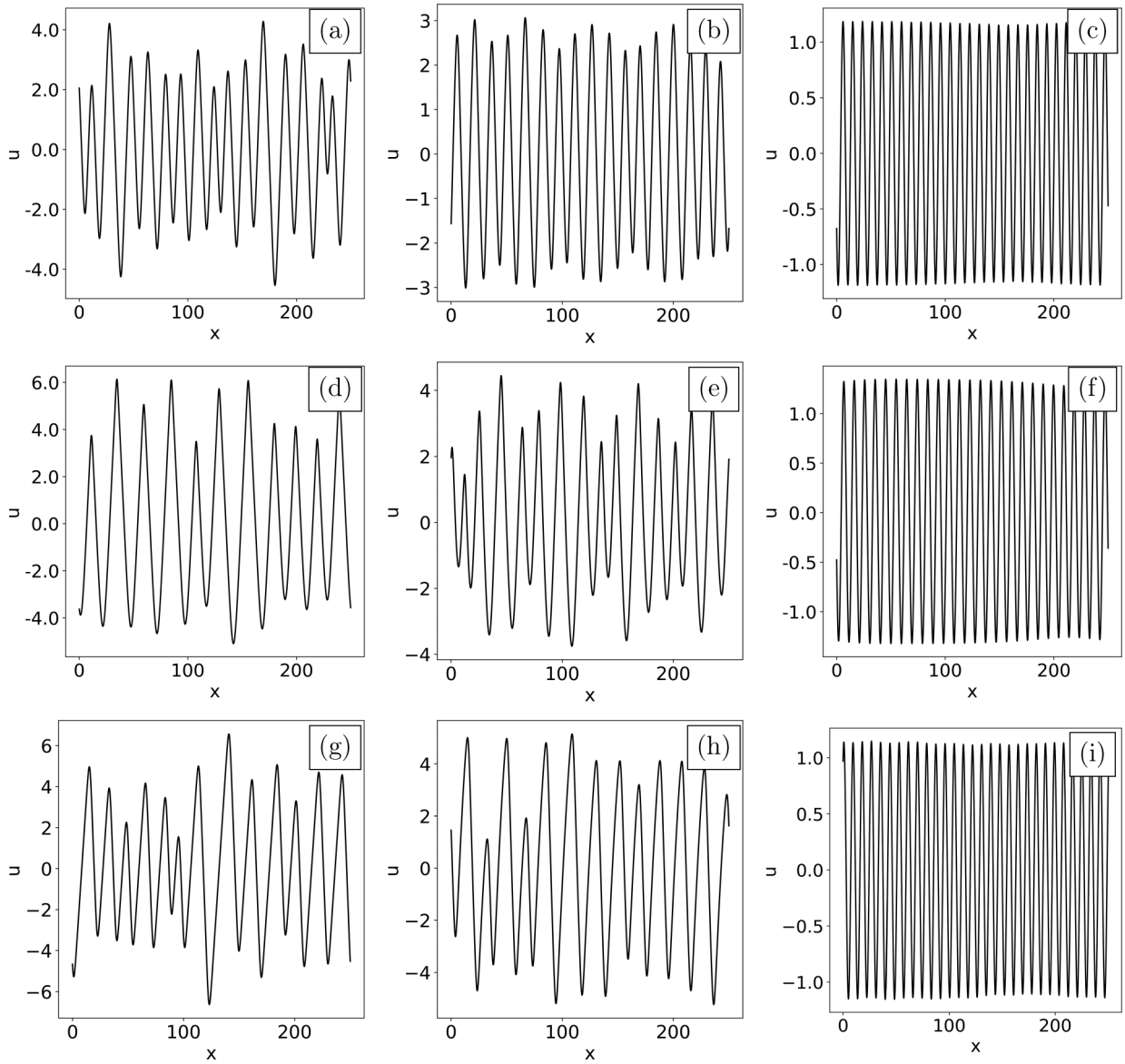

FIG. 2. Plots of the surface height u vs x at $t = 1500$ obtained from integration of Eq. (23) with the following parameter values. Top: $r = \kappa = 0$ and (a) $\gamma = 0$, (b) $\gamma = 1$, (c) $\gamma = 10$. Middle: $r = 1$, $\kappa = 0$ and (d) $\gamma = 0$, (e) $\gamma = 1$, (f) $\gamma = 10$. Bottom: $r = 0$, $\kappa = 1$ and (g) $\gamma = 0$, (h) $\gamma = 1$, (i) $\gamma = 10$. The domain size is 250 for all cases.

in Eq. (42) solve for the values of the constants B_0, B_1, B_2, and B_3. This leads us to the conclusion that

$$u = A_0 \cos(k\xi) + \varepsilon\left[-\tfrac{1}{6}\kappa A_0^2 \cos(2k\xi) + \tfrac{1}{3} rkA_0^2 \sin(2k\xi) + \tfrac{1}{32} kA_0^3 \sin(3k\xi)\right] + O(\varepsilon^2), \tag{44}$$

where the irrelevant constant term εB_0 has been dropped from the right-hand side. Equation (44) shows that for large γ, the steady-state solution is a sinusoid plus a small correction term. The wave number is k, and it is related to the amplitude of the steady-state solution A_0 by Eq. (39).

Combining Eqs. (39) and (41), we see that the propagation velocity v can be written

$$v = \gamma k^2 + O(\varepsilon). \tag{45}$$

The dispersion relation for the linearized EOM is given by $v = \gamma k^2$ for sinusoidal waves with wave vector $\boldsymbol{k} = k\hat{\boldsymbol{x}}$. Equation (45) therefore shows that the nonlinear terms in the full EOM (22) make higher-order contributions to the dispersion relation.

There is a solution to the EOM (22) of the form Eq. (44) for arbitrary amplitudes A_0. The wave number and velocity of the propagating wave are related to A_0 by Eqs. (39) and (41), respectively.

Although we have found approximately sinusoidal traveling wave solutions to the EOM (22) when γ is large for all amplitudes A_0, there is no guarantee that a solution to Eq. (22) with a low amplitude spatial white noise initial condition will converge to a sinusoidal traveling wave solution at long times. Moreover, even if this does happen, we do not know *a priori* which value of A_0 will be selected. To address these issues, we carried out simulations of the EOM (22).

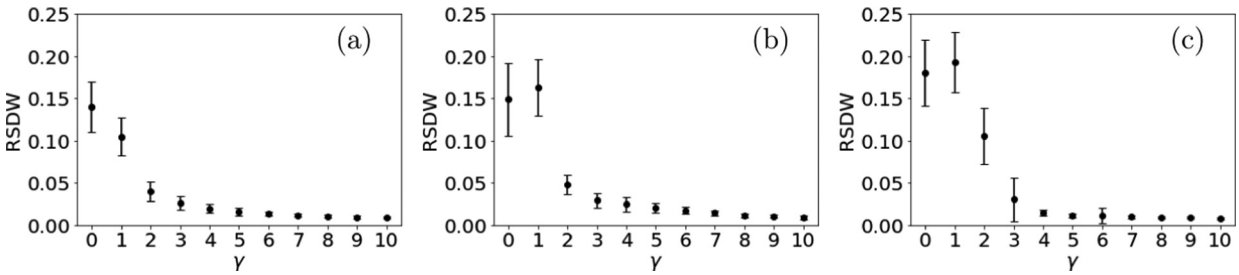

FIG. 3. Plots of the RSDW vs γ at $t = 1000$ obtained from simulations of Eq. (23) with (a) $r = 0$ and $\kappa = 0$, (b) $r = 1$ and $\kappa = 0$, and (c) $r = 0$ and $\kappa = 1$. The domain size was 250.

B. Simulations in one dimension

To begin, we will study the 1D EOM (23). We integrated this PDE numerically using the fourth-order Runge-Kutta exponential time-differencing method described by Cox and Matthews [49] on the domain $0 \leqslant x \leqslant L$ and employed periodic boundary conditions. An initial condition of spatial white noise with amplitude 0.001 was used. The linear terms were computed in Fourier space, and the nonlinear terms in real space. A central finite differencing scheme accurate to fourth order in the grid spacing was used to compute the nonlinear terms.

Figure 2 shows plots of the surface at time $t = 1500$ for several representative choices of γ, r, and κ. This figure strongly suggests that cases in which γ is much larger than r and κ produce surfaces with a much higher degree of order than cases in which γ is zero or comparable in magnitude to the other two parameters. This observation is confirmed by a quantitative analysis, as we will see momentarily.

For a given set of parameters γ, r, and κ, we carried out multiple simulations. We computed the distances between pairs of adjacent peaks and between pairs of adjacent troughs in each simulation. The average interextremum distance in the simulations is an estimate of the mean wavelength Λ. We also computed the standard deviation of the interextremum distances and divided it by Λ to give the relative standard deviation of the wavelength (RSDW). The RSDW is a measure of the degree of order in the ripple pattern; it is small if the pattern is highly ordered and large if it is not.

The RSDW was computed at time $t = 1000$ and was averaged over 100 runs for each set of parameters we studied. The results are plotted versus γ for three choices of r and κ in Fig. 3. In each case, the distribution of interextremum distances becomes narrow and the ripples become highly ordered as γ becomes large. Interestingly, for the cases in which $r \neq 0$ or $\kappa \neq 0$, the degree of order initially deteriorates as γ is increased from zero, but then steadily improves.

Our analysis of the steady states of Eq. (23) given in Sec. VI A suggests that if γ is sufficiently large, the surface is approximately sinusoidal at long times. The power spectral densities (PSDs) shown in Fig. 4 confirm this: sharp peaks appear in the PSDs at a certain wave number k for relatively large γ but not for $\gamma = 0$. For the case with $\gamma = 10$, $r = 1$, and $\kappa = 0$, a small peak can be discerned at a value of k approximately equal to $2k$, in accord with Eq. (44).

Additional evidence that the surface is approximately sinusoidal at long times if γ is sufficiently large is given in Fig. 5. This figure shows the slope distributions of the simulated surfaces at $t = 1000$, averaged over 100 runs. Each

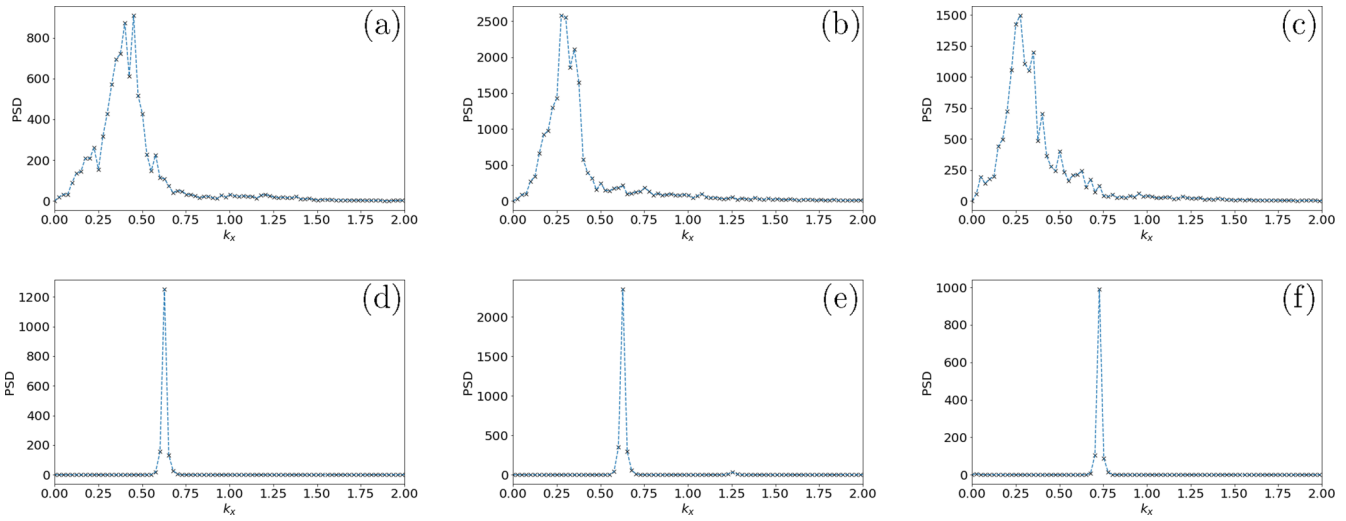

FIG. 4. PSDs for single simulations of Eq. (23) at $t = 1500$. Top: $\gamma = 0$ and (a) $r = \kappa = 0$, (b) $r = 1$ and $\kappa = 0$, and (c) $r = 0$ and $\kappa = 1$. Bottom: $\gamma = 10$ and (d) $r = \kappa = 0$, (e) $r = 1$ and $\kappa = 0$, and (f) $r = 0$ and $\kappa = 1$. The black crosses are the actual data points, and the blue dashed curves are guides to the eye. The domain size was 250.

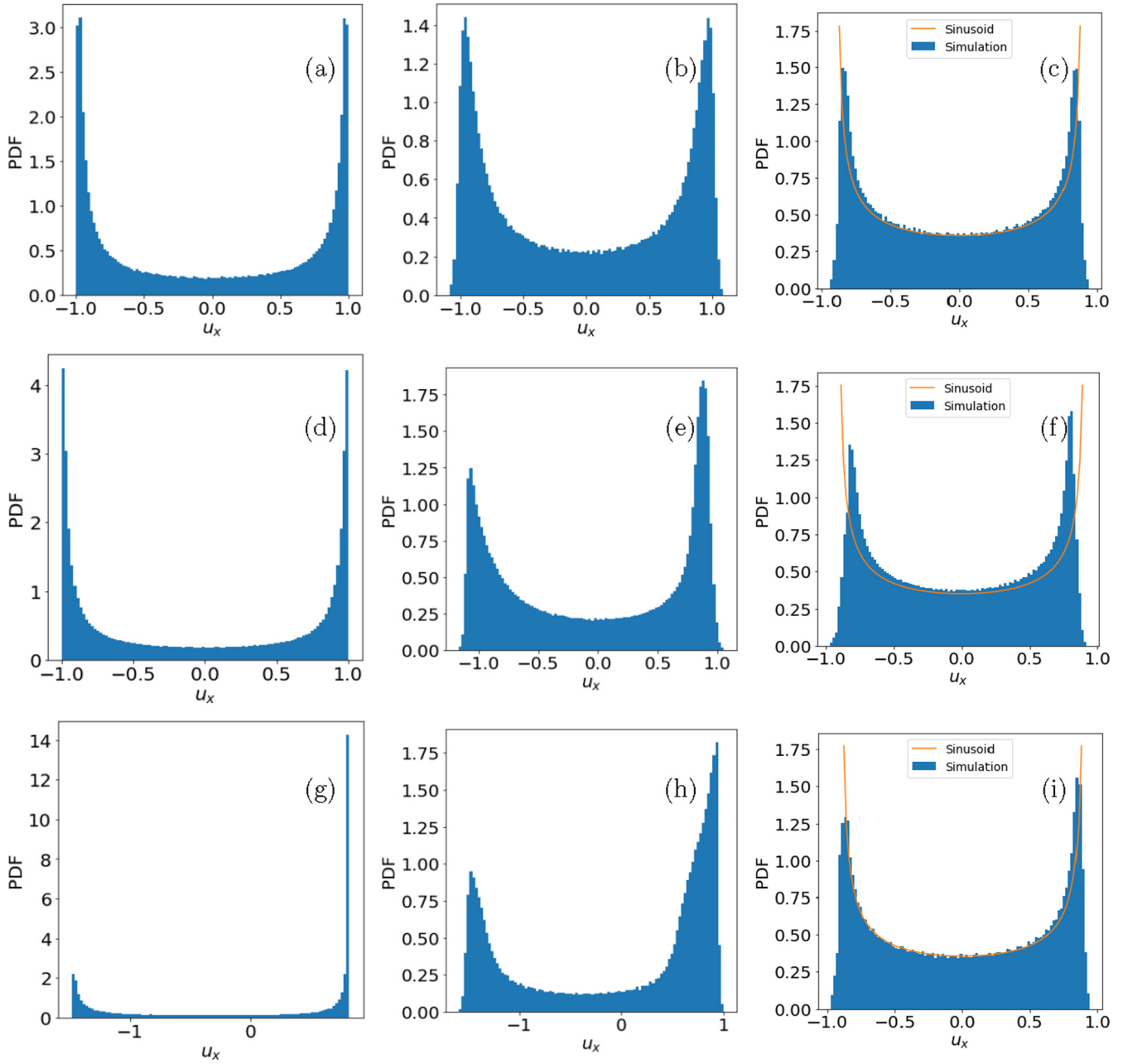

FIG. 5. Slope distributions obtained from simulations of Eq. (23) at time $t = 1000$. Top row: $r = 0$, $\kappa = 0$ and (a) $\gamma = 0$, (b) $\gamma = 1$, and (c) $\gamma = 10$. Middle row: $r = 1$, $\kappa = 0$ and (d) $\gamma = 0$, (e) $\gamma = 1$, and (f) $\gamma = 10$. Bottom row: $r = 0$, $\kappa = 1$ and (g) $\gamma = 0$, (h) $\gamma = 1$, and (i) $\gamma = 10$. The domain size was 250. For each of the three cases with $\gamma = 10$, the PDF is close to the slope distribution of a sinusoid with a wavelength and amplitude equal to the average values of these quantities in the corresponding simulations. The latter distribution is shown in orange.

distribution has been normalized so that the area under the histogram is equal to unity, which converts them into probability distribution functions (PDFs). For each of the three cases with $\gamma = 10$, the PDF is close to the slope distribution of a sinusoid with a wavelength and amplitude equal to the average values of these quantities in the corresponding simulations.

As we saw in Sec. V, most of the surface has a slope close to one of two selected values for $\gamma = r = 0$. This is in accord with the slope distributions in Figs. 5(a) and 5(g), both of which display sharp peaks at two values of the slope. These peaks broaden considerably as γ is increased and the surface approaches a sinusoidal form.

According to the perturbation expansion, the wave number k and the amplitude A_0 are related by Eq. (39) in the steady state. To test this prediction, we took k to be the wave number of the Fourier mode with the largest amplitude and A_0 to be the amplitude of this mode. Different spatial white noise initial conditions lead to different values of k and A_0, and so the values of these quantities were recorded separately for each

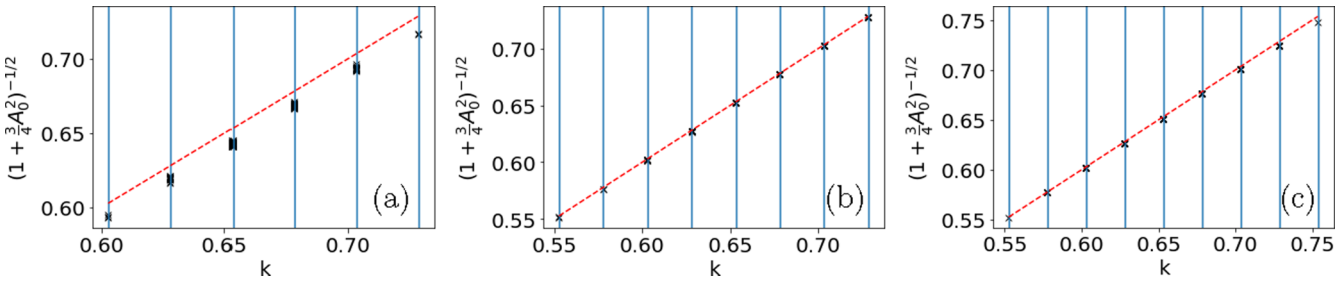

FIG. 6. Plots of the quantity $(1+\frac{3}{4}A_0^2)^{-1/2}$ vs k with values of k and A obtained at $t = 1000$ from simulations of Eq. (23) with (a) $\gamma = 10$, (b) $\gamma = 50$, and (c) $\gamma = 100$. $r = \kappa = 0$ in all cases. The domain size was 250, and 100 simulations were carried out in each case. Each black cross represents the measurements of a single simulation.

simulation we carried out. $(1+\frac{3}{4}A_0^2)^{-1/2}$ is plotted against k at time $t = 1000$ for $r = \kappa = 0$ and three different values of γ in Fig. 6. Each data point represents a single simulation. The vertical lines correspond to values of k that are allowed by the periodic boundary conditions—specifically, the lines show the values $k = 2\pi n/L$, where n is the number of wavelengths present on the surface, and L is the domain size. The dashed red line shows the expected linear relationship. The agreement improves as γ increases and is quite impressive for $\gamma = 100$. This is to be expected, since the perturbation expansion is an expansion in powers of $\varepsilon \equiv 1/\gamma$.

The perturbation expansion also predicts how the propagation velocity v depends on the wave number k in the steady state—see Eq. (45). The value of k in our simulations was determined as described in the preceding paragraph. We computed the velocity of the ripples by measuring the rate of change of the phase of the Fourier transform of $u(x,t)$ for the wave number k. Figure 7 shows v plotted against γk^2, with each data point representing a single simulation. v and k were measured at $t = 1500$. The dashed red line is $v = \gamma k^2$, the leading-order term in the perturbation expansion for the velocity. The agreement is excellent, even for values of γ that are not large.

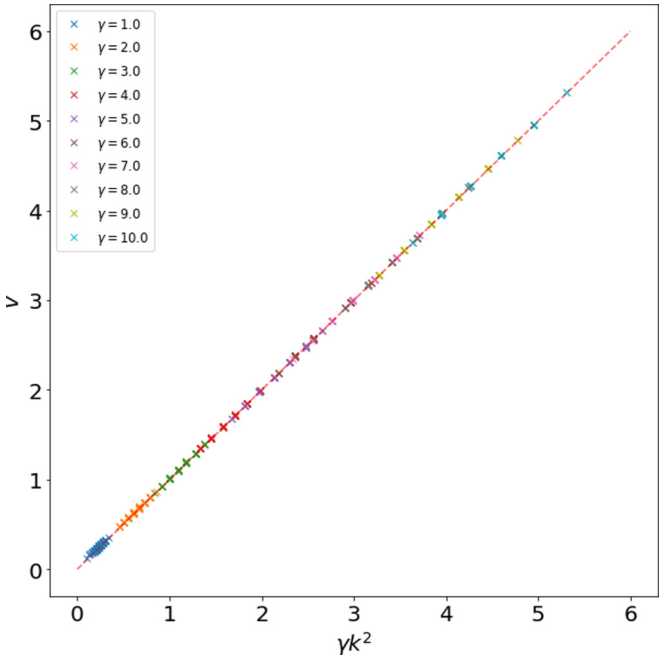

FIG. 7. Plot of v vs γk^2 at time $t = 1500$ for simulations of Eq. (23) with $r = \kappa = 0$. The domain size was 250. The dashed red line is $v = \gamma k^2$.

As we have seen, for $\gamma = r = \kappa = 0$, the EOM (23) is equivalent to the 1D CH equation. In this case, surface ripples coarsen indefinitely, i.e., the surface width w and the mean wavelength Λ increase for all times. (The coarsening does, however, become logarithmically slow at long times [50].) As Figs. 8 and 9 show, for nonzero γ, dispersion slows or even arrests the coarsening that would otherwise occur. This remains true if r or κ is nonzero provided that γ is sufficiently large. Once again, this is consistent with the perturbation expansion, since for large γ and at long times, the surface approaches an approximately sinusoidal form that propagates without significantly changing its shape.

Although the surface evolves into a highly ordered sinusoidal form when γ is large relative to r and κ, its behavior is decidedly different if κ is comparable in magnitude to γ. As illustrated by Fig. 10, in this case the term $\kappa\partial_x u_x^2$ destroys the high degree of order that would exist in its absence.

C. Simulations in two dimensions

Because the term u_{yy} in the 2D EOM (22) tends to smooth out any variations of u in the y direction, the behavior of the 2D EOM is in most respects quite similar to that of the 1D EOM (23). We will therefore only briefly discuss the behavior of the solutions to the 2D EOM.

In Fig. 11, plots of the surface at time $t = 1500$ for several representative choices of γ, r and κ are shown. As in 1D, cases in which γ is significantly larger than r and κ produce surfaces with a much higher degree of order than cases in which γ is zero or comparable in magnitude to the other two parameters. Further evidence that supports this conclusion is provided by plots of the RSDW versus γ. These plots are not reproduced here since they look very much like the corresponding plots in 1D (Fig. 3).

The PSDs at time $t = 1000$ in Fig. 12 have sharp peaks for relatively large γ, confirming that just as in 1D, in 2D the surface is approximately sinusoidal at long times if γ is sufficiently large. As before, sharp peaks do not appear for $\gamma = 0$. Distributions of the slope u_x for simulations in 2D are similar to those shown in Fig. 5 for 1D and are not included for the sake of brevity. They provide additional support for the conclusion that the surface is approximately sinusoidal at

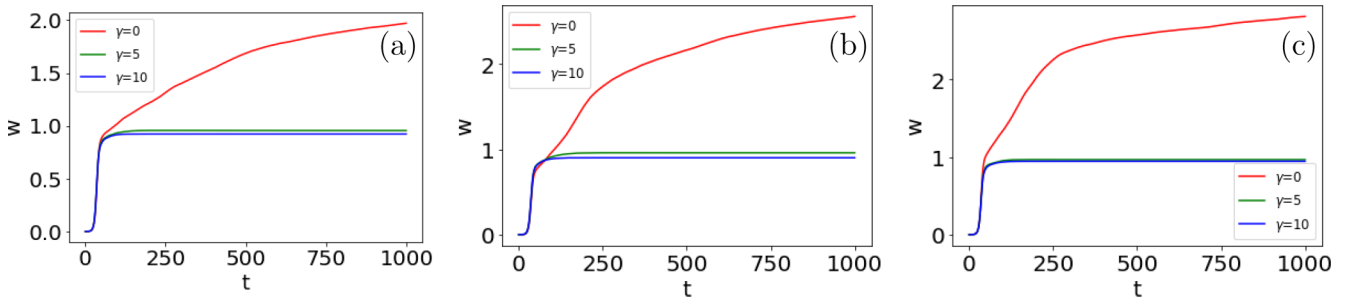

FIG. 8. Plots of the RMS surface width w vs t obtained from simulations of Eq. (23) with (a) $r = 0$ and $\kappa = 0$, (b) $r = 1$ and $\kappa = 0$, and (c) $r = 0$ and $\kappa = 1$. The domain size was 250 and an average over 100 simulations was taken.

long times if γ is sufficiently large. As in 1D, plots of w and Λ versus time (not shown) demonstrate that dispersion slows or stops coarsening.

Although the dynamics are in many ways similar in one and two dimensions, there is an aspect of the dynamics in 2D that occurs for relatively large γ that does not have a 1D analog. In 2D, as time passes, multiple band-shaped regions develop in which the ripples are highly ordered, as shown in Fig. 13(a), for example. These bands are roughly aligned with the x direction. Each pair of adjacent bands is separated by a unique type of defect that we will refer to as a "seam." Typically, the number of wavelengths on either side of a seam differ by one. A seam can therefore be thought of as a dislocation that is spread out along the x direction. Analogous defects occur in the anisotropic Kuramoto-Sivashinsky equation with an added strongly dispersive term [18]. Clearly, seams are a feature of the 2D dynamics that have no 1D counterpart.

Seams travel either parallel or anti-parallel to the y direction, toward the region with the shorter wavelength, as illustrated by Fig. 13. When two seams meet, they either combine to form a new seam or, as in Fig. 13, annihilate. Ultimately, no seams remain and a defect-free, highly ordered ripple pattern remains.

To compare the results of our simulations in 2D with the predictions of the perturbation expansion, we made 1D cuts of the surface along the x direction at several equally spaced values of y. These cuts are shown on the surfaces in Fig. 14. We calculated the quantities A_0, k_x and v for each cut in precisely the same way that we found these quantities for our simulations in 1D.

The surfaces in the top row of Fig. 14 come from a simulation of Eq. (22) with $\gamma = 50$ and $r = \kappa = 0$ and are at times $t = 100$, 250, and 1000. In the second row of the figure, the quantity $(1 + \frac{3}{4}A_0^2)^{-1/2}$ is plotted versus the wave number k_x for the surface above it. One point was plotted for each cut. Because one or more points could lie atop one another, we made the darkness of the crosses proportional to the number of points that exactly coincided. At time $t = 100$, some of the points in Fig. 14(d) do not agree with the perturbation theory prediction, which is shown with a blue line. These points come from cuts that happen to run through or near a seam. Because the ripple amplitude is reduced in magnitude within a seam, these points lie above the perturbation theory prediction. At time $t = 250$, the agreement between the data and the prediction is better, as seen in Fig. 14(e). Finally, at time $t = 1000$, no seams remain and the agreement is excellent. A steady state has very nearly been achieved at this time, and so the agreement with the approximate steady-state solution found using perturbation theory is to be expected.

There is an interesting sidelight to Figs. 14(d)–14(f). At times $t = 100$ and 250, there are two different values of k_x in which the agreement between the perturbation theory prediction and the simulation is very good. The reason for this is that there are two bands of y values with different values of k_x where the ripple amplitude is close to the value predicted by perturbation theory.

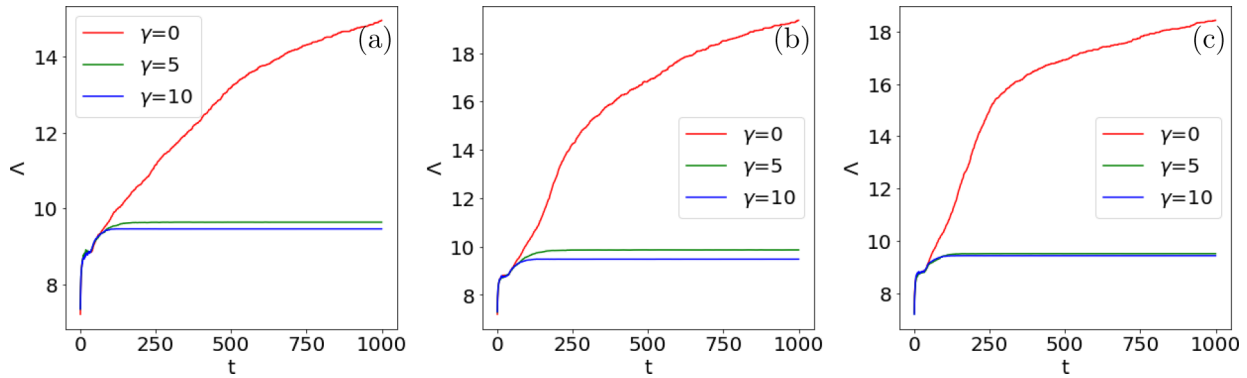

FIG. 9. Plots of the wavelength Λ vs t obtained from simulations of Eq. (23) with (a) $r = 0$ and $\kappa = 0$, (b) $r = 1$ and $\kappa = 0$, and (c) $r = 0$ and $\kappa = 1$. The domain size was 250 and an average over 100 simulations was taken.

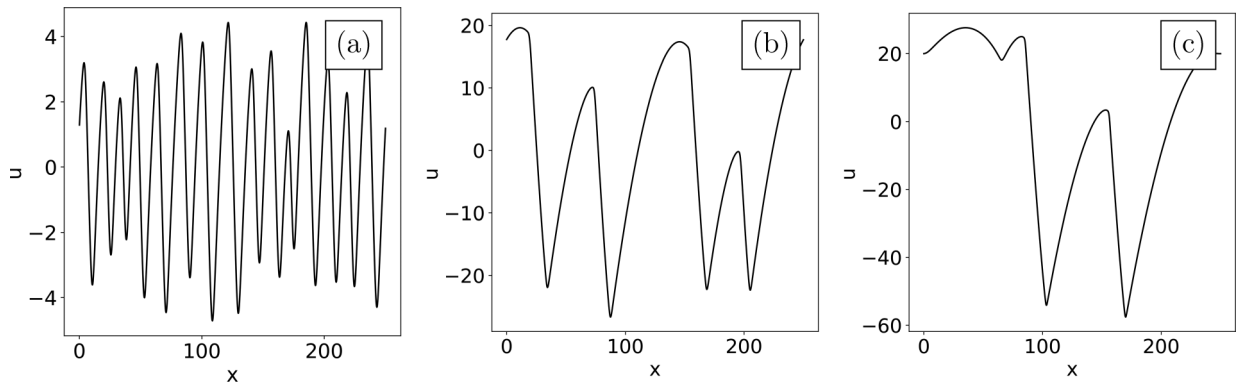

FIG. 10. Plots of the surface height u vs x at $t = 750$ obtained from integration of Eq. (23) with $r = 0$ and (a) $\kappa = \gamma = 1$, (b) $\kappa = \gamma = 3$, and (c) $\kappa = \gamma = 5$. The domain size is 250 for all cases.

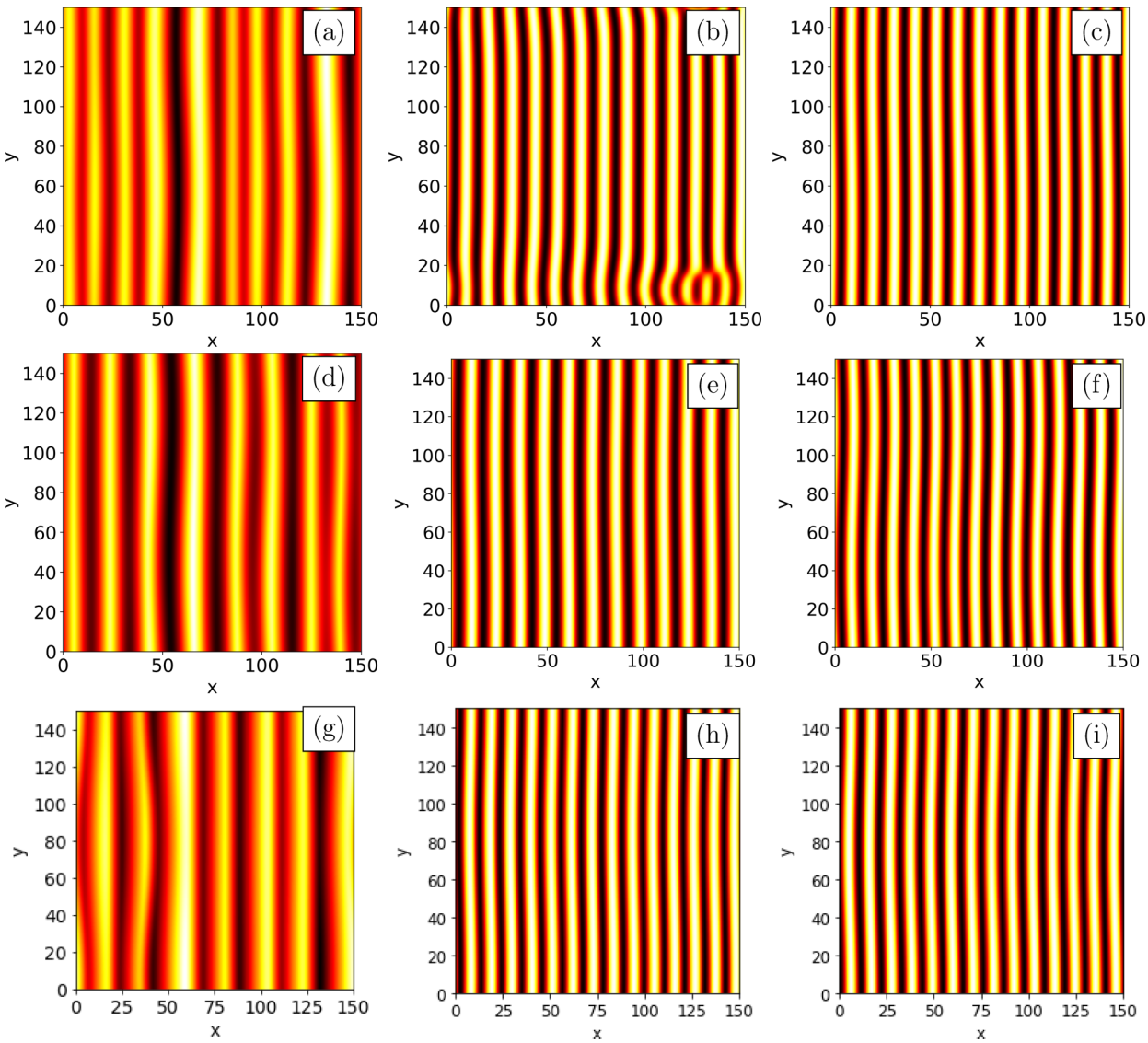

FIG. 11. Plots of the surface height u at $t = 1500$ obtained from integration of Eq. (22). Top row: $r = \kappa = 0$ and (a) $\gamma = 0$, (b) $\gamma = 5$, (c) $\gamma = 10$. Middle row: $r = 1$, $\kappa = 0$ and (d) $\gamma = 0$, (e) $\gamma = 5$, (f) $\gamma = 10$. Bottom row: $r = 0$, $\kappa = 1$ and (g) $\gamma = 0$, (h) $\gamma = 5$, (i) $\gamma = 10$. The domain size was 150×150 for all cases.

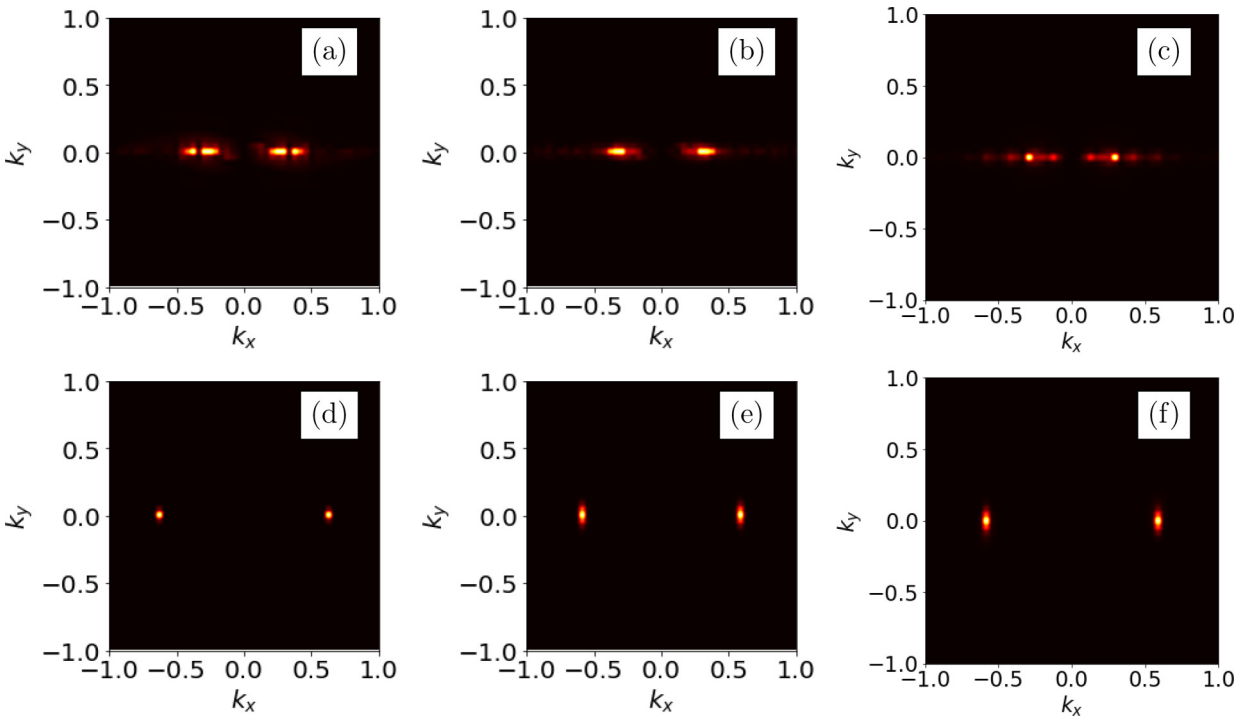

FIG. 12. PSDs of the surface for single simulations of Eq. (22) at $t = 1000$. Top row: $\gamma = 0$ and (a) $r = 0$ and $\kappa = 0$, (b) $r = 1$ and $\kappa = 0$, and (c) $r = 0$ and $\kappa = 1$. Bottom row: $\gamma = 10$ and (d) $r = 0$ and $\kappa = 0$, (e) $r = 1$ and $\kappa = 0$, and (f) $r = 0$ and $\kappa = 1$. The domain size was 150×150 in all six cases.

The velocity v is plotted versus γk_x^2 for the surface above it in Figs. 14(g)–14(i). Even at times $t = 100$ and 250, when defects still remain in the patterns and there are bands of ripples with different wave numbers, the agreement between the simulations and the perturbation theory prediction is very good. The defects have all disappeared by $t = 1000$, and the points from all of the cuts very nearly coincide with each other and the perturbation theory prediction.

To test the perturbation theory prediction for the dependence of the ripple velocity on γ, we simulated Eq. (22) until time $t = 1000$ for $r = \kappa = 0$ and a selection of γ values. Five simulations were carried out for each choice of parameters. The results are shown in Fig. 15. In this figure, points were plotted for each 1D cut and each simulation, but this is not apparent because the points for each choice of parameters very nearly lie on top of one another. The agreement with the leading-order prediction of perturbation theory, $v = \gamma k_x^2$, is excellent even for γ as small as two.

As in 1D, when κ is comparable in magnitude to γ, nonlinear dispersion disrupts the high degree of order that would prevail if it were not present. This is illustrated by Fig. 16.

VII. DISCUSSION

Suppose a solid surface is sputtered by an obliquely incident noble gas ion beam and that a layer at the surface of the solid is amorphized by the bombardment. It was shown in recent work that for angles of ion incidence θ just above the threshold angle for pattern formation θ_c, linear dispersion strongly affects the dynamics and highly ordered ripples form [20]. That work suggests that in the problem studied in the current paper, linear dispersion could lead to

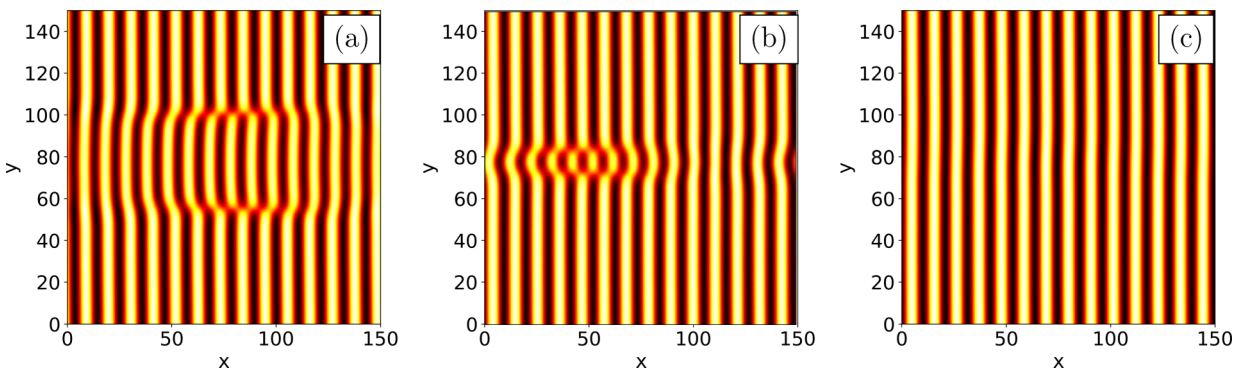

FIG. 13. Plot of the surface height u at (a) $t = 400$, (b) $t = 755$, and (c) $t = 800$ for the case with $\gamma = 50$, $r = 0$, and $\kappa = 0$.

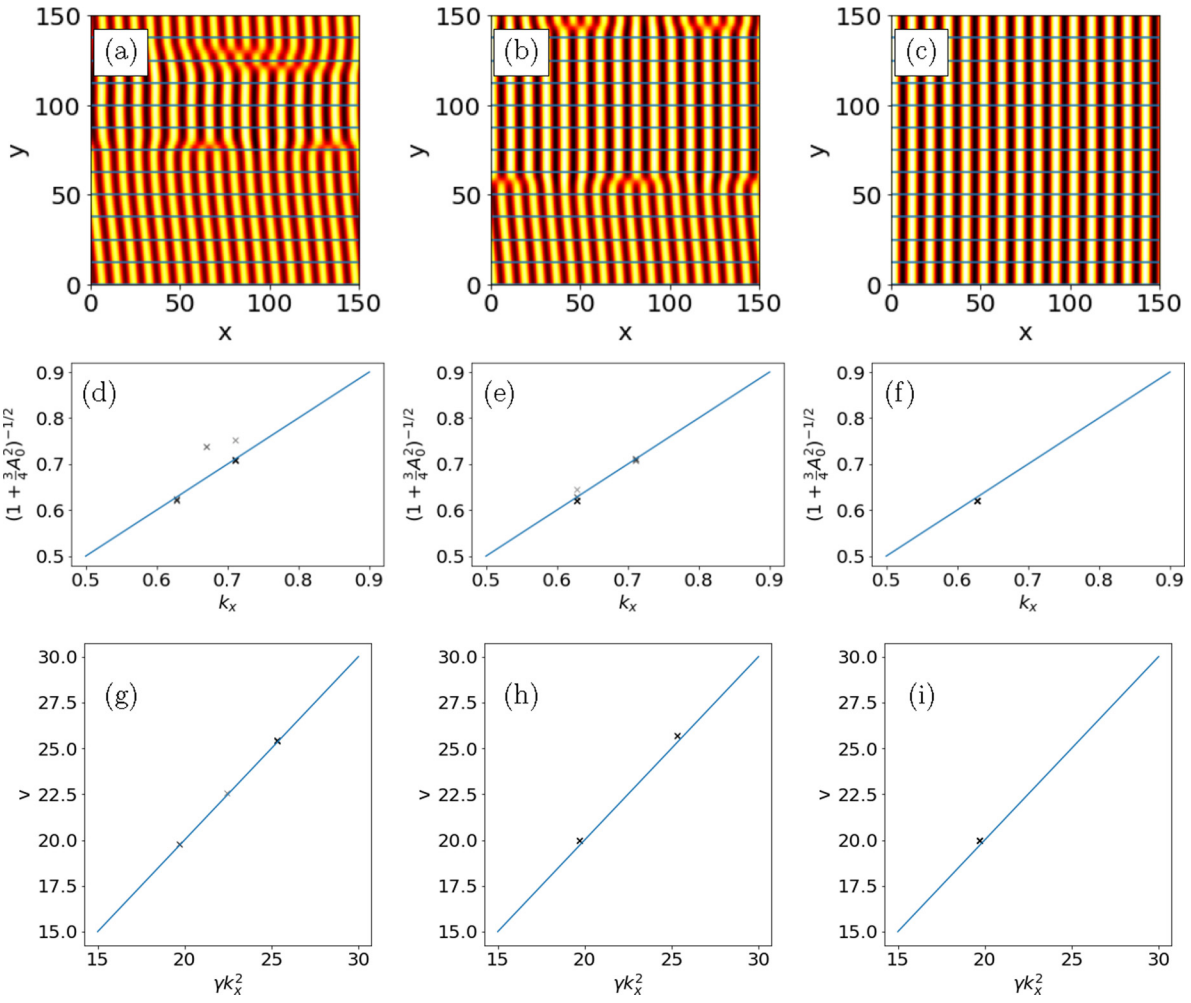

FIG. 14. Top row: Plots of the surface height u for simulations of Eq. (22) with $r = \kappa = 0$ and $\gamma = 50$ at (a) $t = 100$, (b) $t = 250$, and (c) $t = 1000$. The domain size was 150×150, and horizontal lines are drawn to show where cuts were made. Each cut yields one point in each of the corresponding plots. Middle row: Plots of the quantity $(1 + \frac{3}{4}A_0^2)^{-1/2}$ vs k_x at (d) $t = 100$, (e) $t = 250$, and (f) $t = 1000$. Bottom row: Plots of v vs γk_x^2 at (g) $t = 100$, (h) $t = 250$, and (i) $t = 1000$. In both the middle and bottom rows, the blue lines show the perturbation theory predictions.

highly ordered ripples close to the the critical temperature T_c when there is a nonzero miscut angle ψ. This is because the coefficient γ of the linearly dispersive term in Eq. (22) becomes large as T approaches T_c from above. However, for highly ordered, nearly sinusoidal ripples to develop, γ must be large compared to r, 1, *and* the coefficient of the nonlinearly dispersive term κ. To ensure that γ is much larger than κ, the angle of ion incidence θ must be chosen appropriately. Once this has been done, ion bombardment will produce highly ordered, nearly sinusoidal ripples.

To identify the angle θ that leads to highly ordered ripples in an experiment, a shortcut could be employed. In particular, the (001) surface of GaAs with a given miscut angle ψ could be bombarded with a broadly divergent ion beam at nominal normal incidence. In this way, by imaging the surface at different points, the effect of bombarding with a range of angles of incidence could be determined. Once the appropriate value of θ has been determined, highly ordered ripples could be produced in future experiments using a collimated ion beam with this angle of incidence.

From a mathematical point of view, in earlier work it was shown that if a sufficiently strong linearly dispersive term is added to the 1D Kuramoto-Sivashinsky equation, then ripples with a high degree of order will develop [25]. In the present paper, we have shown that if a sufficiently strong linearly dispersive term is appended to the 1D CH equation for a critical quench, then a highly ordered pattern will emerge. However, a pattern with a high degree of order does not necessarily result when a strong linearly dispersive term is added to the 1D CH equation for a off-critical quench,

$$\phi_t = \partial_x^2(a\phi + b\phi^2 + \alpha\phi^3 - B\phi_{xx}). \tag{46}$$

This is due to the presence of the term $b\partial_x^2\phi^2$.

A natural question to ask is whether our theory could be applied to other surfaces besides the (001) surface of GaAs. At the present time, highly ordered ripples are known to form on only one other surface that remains crystalline when it is bombarded at normal incidence: the (001) surface of InAs [14]. However, it is not known whether InAs is amorphized by ion bombardment below a temperature T_R. If there is such a temperature T_R, then it is below room temperature

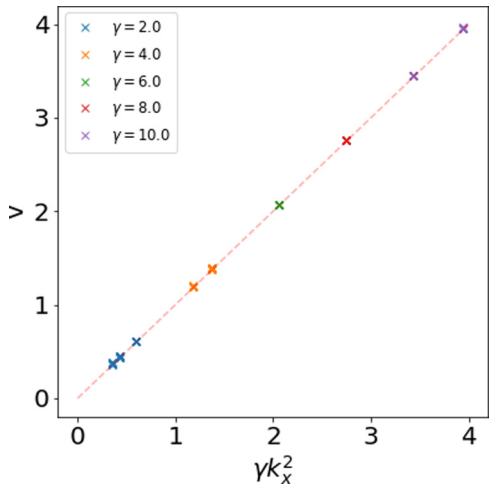

FIG. 15. v plotted versus γk_x^2 at time $t = 1000$ for simulations of Eq. (22) with the parameter values $r = 0$, $\kappa = 0$, and γ as indicated. Five simulations were carried out for each value of γ. Each data point represents a cut from a single simulation, but the points for each choice of parameters very nearly lie on top of one another. The dashed red line shows $v = \gamma k_x^2$, the leading-order term in the perturbation expansion for the velocity. The domain size was 150×150.

[45]. In addition, it has not yet been determined whether highly ordered ripples form on InAs if the incident ions have an energy below the sputtering threshold. If it turns out that there is recrystallization temperature T_R and highly ordered ripples form on InAs when it is bombarded with low-energy ions at a temperature $T > T_R$, then our theory will apply.

In the past, an imprecise analogy has often been made between nanoscale surface ripples produced by oblique-incidence ion bombardment of solid surfaces and aeolian sand dunes (see Ref. [51], for example). For ion bombardment of solids in the high energy regime, however, the analogy is actually rather poor: incident ions move ballistically until they reach the surface of the solid but air flows hydrodynamically over a dune. In addition, the sputtering produced by the impinging ions leads to nonlinear terms in the EOM that do not conserve mass. In contrast, the mass is conserved in the dynamics of aeolian sand dunes and therefore terms of this kind do not appear in the EOM.

The analogy becomes much stronger when a crystalline solid is bombarded in the low-energy regime in which sputtering does not occur because then mass is conserved. In the case of a miscut GaAs target, we have shown that the EOM is Eq. (22) for temperatures T just above the critical temperature $T_{c,0}$ and for small miscut angles. Precisely this EOM has been studied as a model of the dynamics of aeolian sand dunes [52,53]. In that model, u is the height of the sand surface, the x axis points in the direction of the wind, and the y direction is the transverse horizontal direction.

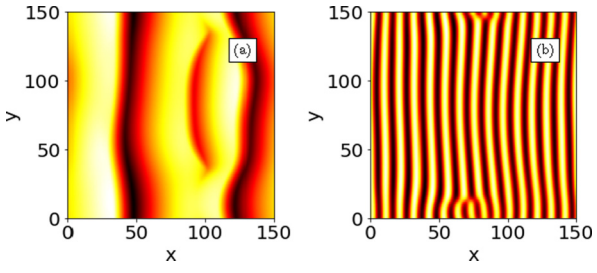

FIG. 16. Simulations of Eq. (22) at $t = 500$ with the parameter values (a) $r = 0$ and $\kappa = \gamma = 3$ and (b) $r = \kappa = 0$ and $\gamma = 3$. The domain size was 150×150.

The EOM (22) studied in this paper is actually quite generic. In addition to being used as a model of aeolian sand dunes, the version that has $\gamma = \kappa = 0$ has been employed as a model of surface ripple formation during thin film deposition with diametrically opposed, obliquely incident broad atomic beams [47] and as a model of pattern formation on solid surfaces bombarded by two broad ion beams in the regime in which sputtering is negligible [54].

VIII. CONCLUSIONS

When the (001) surface of a GaAs single crystal is bombarded with a normally-incident, low-energy noble gas ion beam and the sample temperatures T is close to the threshold temperature for pattern formation $T_{c,0}$, highly ordered, faceted ripples with their wave vector aligned with the [110] direction form. Because the wavelength can vary along the [110] direction, these ripples are not perfectly ordered.

Two additional terms appear in the equation of motion when there is a miscut along the [110] direction, a linearly dispersive term and a nonlinear dispersion term. The coefficients of both of these terms can become large as the threshold temperature is approached from above. In the absence of strong nonlinear dispersion, strong linear dispersion leads to very highly ordered ripples. These ripples are not faceted, but instead have a nearly sinusoidal profile even though they are on the surface of a single crystal. In general, this order is disrupted by nonlinear dispersion. However, the effect of nonlinear dispersion can be made negligibly small by choosing the angle of incidence appropriately. If that is done, then ion bombardment will lead to the formation of highly ordered ripples with a nearly sinusoidal profile.

We also found an interesting special case in which the linearly dispersive and the conserved Kuramoto-Sivashinsky terms do not appear in the equation of motion. In this case, depending on the values of the parameters, either nucleation and growth of facets or spinodal decomposition can occur.

As mentioned in the Introduction, Chowdhury and Ghose have bombarded the (001) surface of GaAs with a normally incident, low-energy noble gas ion beam [24]. The sample temperature T was not close to the threshold temperature for pattern formation $T_{c,0}$, however, and so a comparison between the results of these experiments and our theoretical predictions for the case $\theta = \psi = 0$ cannot be made.

To date, no systematic studies of the ion bombardment of the (001) surface of GaAs with a miscut have appeared in print. Because a rich variety of phenomena could result—including the formation of highly ordered, nearly sinusoidal ripples, nucleation and growth of facets, and spinodal decomposition—experiments of this kind would likely lead to fascinating results as well as providing a test of the theory presented in this paper.

ACKNOWLEDGMENTS

We are grateful to Debasree Chowdhury, Debabrata Ghose, Denise Erb, Stefan Facsko, and Patrick Shipman for valuable discussions. This work was supported by Grants No. DMS-1814941 and No. DMR-2116753 awarded by the U.S. National Science Foundation.

[1] J. Muñoz-García, L. Vázquez, M. Castro, R. Gago, A. Redondo-Cubero, A. Moreno-Barrado, and R. Cuerno, Mater. Sci. Eng. R **86**, 1 (2014).
[2] S. Facsko, T. Dekorsy, C. Koerdt, C. Trappe, H. Kurz, A. Vogt, and H. L. Hartnagel, Science **285**, 1551 (1999).
[3] F. Frost, A. Schindler, and F. Bigl, Phys. Rev. Lett. **85**, 4116 (2000).
[4] R. M. Bradley and P. D. Shipman, Phys. Rev. Lett. **105**, 145501 (2010).
[5] P. D. Shipman and R. M. Bradley, Phys. Rev. B **84**, 085420 (2011).
[6] R. M. Bradley and P. D. Shipman, Appl. Surf. Sci. **258**, 4161 (2012).
[7] A. Cuenat, H. B. George, K.-C. Chang, J. M. Blakely, and M. J. Aziz, Adv. Mater. **17**, 2845 (2005).
[8] B. Ziberi, F. Frost, T. Höche, and B. Rauschenbach, Phys. Rev. B **72**, 235310 (2005).
[9] A. Keller and S. Facsko, Phys. Rev. B **82**, 155444 (2010).
[10] F. C. Motta, P. D. Shipman, and R. M. Bradley, J. Phys. D **45**, 122001 (2012).
[11] M. P. Gelfand and R. M. Bradley, Phys. Rev. B **86**, 121406(R) (2012).
[12] S. A. Mollick, D. Ghose, P. D. Shipman, and R. M. Bradley, Appl. Phys. Lett. **104**, 043103 (2014).
[13] K. Zhang, O. Bobes, and H. Hofsäss, Nanotechnology **25**, 085301 (2014).
[14] X. Ou, K.-H. Heinig, R. Hübner, J. Grenzer, X. Wang, M. Helm, J. Fassbender, and S. Facsko, Nanoscale **7**, 18928 (2015).
[15] D. Chowdhury and D. Ghose, Vacuum **129**, 122 (2016).
[16] D. A. Pearson, R. M. Bradley, F. C. Motta, and P. D. Shipman, Phys. Rev. E **92**, 062401 (2015).
[17] M. P. Harrison and R. M. Bradley, Phys. Rev. E **93**, 040802(R) (2016).
[18] K. M. Loew and R. M. Bradley, Phys. Rev. E **100**, 012801 (2019).
[19] D. Chowdhury and D. Ghose, Surf. Interfaces **17**, 100364 (2019).
[20] R. M. Bradley, Phys. Rev. E **102**, 012807 (2020).
[21] S. Jo, J. Jun, E. Lee, S. M. Yoon, J. Seo, J. Muñoz-García, R. Cuerno, and J.-S. Kim, Phys. Rev. B **102**, 045421 (2020).
[22] Comparable results were later reported in Refs. [15] and [19].
[23] Q. Huang, Q. jia, J. Feng, H. Huang, X. Yang, J. Grenzer, K. Huang, S. Zhang, J. Lin, H. Zhou, T. You *et al.*, Nat. Commun. **10**, 2437 (2019).
[24] D. Chowdhury, D. Ghose, S. A. Mollick, B. Satpati, and S. R. Bhattacharyya, Phys. Status Solidi B **252**, 811 (2015).
[25] T. Kawahara, Phys. Rev. Lett. **51**, 381 (1983).
[26] U. Valbusa, C. Boragno, and F. B. De Mongeot, J. Phys.: Condens. Matter **14**, 8153 (2002).
[27] A. Levandovsky and L. Golubović, Phys. Rev. B **69**, 241402(R) (2004).
[28] E. Chason and W. L. Chan, in *Materials Science with Ion Beams*, edited by H. Bernas, Topics in Applied Physics (Springer-Verlag, Berlin, Heidelberg, 2010), Vol. 116, pp. 53–71.
[29] L. Golubović, A. Levandovsky, and D. Moldovan, East Asian J. Appl. Math. **1**, 297 (2011).
[30] G. Carter and V. Vishnyakov, Phys. Rev. B **54**, 17647 (1996).
[31] M. Moseler, P. Gumbsch, C. Casiraghi, A. C. Ferrari, and J. Robertson, Science **309**, 1545 (2005).
[32] B. Davidovitch, M. J. Aziz, and M. P. Brenner, Phys. Rev. B **76**, 205420 (2007).
[33] K. Nordlund, private communication (2015).
[34] R. M. Bradley and J. M. E. Harper, J. Vac. Sci. Technol. A **6**, 2390 (1988).
[35] R. M. Bradley and H. Hofsäss, J. Appl. Phys. **120**, 074302 (2016).
[36] H. Hofsäss, K. Zhang, and O. Bobes, J. Appl. Phys. **120**, 135308 (2016).
[37] S. A. Norris, J. Samela, M. Vestberg, K. Nordlund, and M. J. Aziz, Nucl. Instrum. Meth. B **318**, 245 (2014).
[38] S. A. Norris, J. Samela, M. Vestberg, K. Nordlund, and M. J. Aziz, Nucl. Instrum. Meth. B, **349**, 192 (2015).
[39] C. C. Umbach, R. L. Headrick, and K.-C. Chang, Phys. Rev. Lett. **87**, 246104 (2001).
[40] W. W. Mullins, J. Appl. Phys. **28**, 333 (1957).
[41] J. Villain, J. Phys. I (France) **1**, 19 (1991).
[42] T. C. Kim, C.-M. Ghim, H. J. Kim, D. H. Kim, D. Y. Noh, N. D. Kim, J. W. Chung, J. S. Yang, Y. J. Chang, T. W. Noh, B. Kahng, and J. S. Kim, Phys. Rev. Lett. **92**, 246104 (2004).
[43] M. Castro, R. Cuerno, L. Vázquez, and R. Gago, Phys. Rev. Lett. **94**, 016102 (2005).
[44] M. Sato and M. Uwaha, Europhys. Lett. **32**, 639 (1995).
[45] G. Malsch, Master's Thesis, Technische Universität Dresden, 2017.
[46] J. Muñoz-García, R. Cuerno, and M. Castro, Phys. Rev. B **78**, 205408 (2008).
[47] R. M. Bradley and T. Sharath, J. Appl. Phys. **129**, 175303 (2021).
[48] R. C. Desai and R. Kapral, *Dynamics of Self-Organized and Self-Assembled Structures* (Cambridge University Press, Cambridge, United Kingdom, 2009).
[49] S. M. Cox and P. C. Matthews, J. Comput. Phys. **176**, 430 (2002).
[50] F. Liu and H. Metiu, Phys. Rev. B **48**, 5808 (1993).
[51] T. Aste and U. Valbusa, Physica A **332**, 548 (2004).
[52] Z. Csahók, C. Misbah, F. Rioual, and A. Valance, Eur. Phys. J. E **3**, 71 (2000).
[53] H. Yizhaq, N. J. Balmforth, and A. Provenzale, Physica D **195**, 207 (2004).
[54] R. M. Bradley and T. Sharath, Phys. Rev. E **103**, 022804 (2021).